## Supplementary Information

# Introducing Built-in Electric Field and Anions Active Sites in COFs through Ionic Polarization for Efficient Solar Energy Catalysis

Jiahe Zhang[a,b†], Xiaoning Li[a†], Haijun Hu[b], Hongwei Huang[d], Hui Li[a], Xiaodong Sun*[a,b] and Tianyi Ma*[a]

J. Zhang, Dr. X. Li, Prof. H. Li, Prof. X. Sun, Prof. T. Ma
School of Science, RMIT University, Melbourne, VIC 3000, Australia
E-mail: tianyi.ma@rmit.edu.au

J. Zhang, H. Hu, Prof. X. Sun
Institute of Clean Energy Chemistry, Key Laboratory for Green Synthesis and Preparative Chemistry of Adv. Mater., College of Chemistry, Liaoning University, Shenyang 110036, People's Republic of China
E-mail: sunxiaodong@lnu.edu.cn

Prof. H. Huang
Beijing Key Laboratory of Materials Utilization of Nonmetallic Minerals and Solid Wastes, National Laboratory of Mineral Materials, School of Materials Science and Technology, China University of Geosciences, Beijing, 100083, China

† Those authors contributed equally

**Characterization**

SEM images were acquired using a Hitachi SU-8010 equipped with an EDS analyzer. TEM and HRTEM images were obtained on a JEM-2100 operating at 10 kV. XRD patterns were collected using a D8 Advance (Bruker) X-ray diffraction system with Cu Kα radiation (λ = 0.15406 nm). XPS spectra were recorded by the Thermo Scientific ESCALAB 250Xi spectrometer equipped with a monochromatic Al Kα X-ray source (1486.6 eV). 13C solid-state nuclear magnetic resonance spectra were acquired with Bruker 400M. The UV-vis spectra were obtained by Ultraviolet-visible diffuse reflectance spectroscopy with $BaSO_4$ as the reflectance standard (Shimadzu UV-2550). The surface area and pore size of the prepared samples were investigated by Quanta Autosorb IQ. Fluorescence measurements were carried out with the RF-5301PC (Shimadzu, Japan) fluorescence spectrophotometer (excitation wavelength: 350 nm). Fourier transform infrared spectroscopy was performed on a Nicolet Nexus 670 FT-IR spectrophotometer at a resolution of 4 $cm^{-1}$. Kelvin probe force microscopy (KPFM, Bruker Dimenson Icon) was utilized to ascertain the surface potential of materials. The surface photovoltage test was conducted at room temperature, where the PV signal of the sample was recorded under the excitation of a laser pulse (50 mJ $cm^{-2}$). Fluorescence measurements were carried out with the RF-5301PC (Shimadzu, Japan) fluorescence spectrophotometer.

**Photocatalytic $H_2$ production tests**

Photocatalytic $H_2$ production experiments were conducted using a fully glass automatic online trace gas analysis system (Labsolar-6A, Beijing Perfectlight Technology Co., Ltd.). The light source was a 300 W Xenon lamp with a 42 nm flter (PLS-SXE300/300UV, light intensity: 100 mW·cm$^{-2}$, Beijing Perfectlight Technology Co., Ltd.). Hydrogen detection and quantitative analysis were performed using a GC7900 gas chromatography system (Shanghai Tianmei Scientific Instrument Co.) with nitrogen as the carrier gas, at 30-minute intervals. The catalyst was placed in a custom quartz glass reactor, and the reaction temperature was maintained at 5 ℃ using a water condenser. 10 mg of catalyst was added to 100 mL of deionized water containing 100 mg of L-Ascorbic acid as a hole scavenger. The suspension was then stirred in a 200 mL custom quartz reactor. The suspension was then transferred to the custom quartz reactor for the photocatalytic reaction. Prior to each photocatalytic reaction, the system was vacuum-treated several times to remove dissolved air. The entire reaction system was irradiated with Xe light using a UV cut-off filter ($\lambda \geq 420$ nm). The vertical distance between the Xe lamp and the reactor was approximately 3 cm. Additionally, the apparent quantum efficiency (AQE) was measured using a xenon lamp equipped with bandpass filters. Photocatalytic experiments were performed with 10 mg of catalysts, using filters with wavelengths of 475, 500, 520, 550, and 600 nm, respectively. The specific value of AQE was calculated on the basis of the

following formula:

$$AQE(H_2)\% = \frac{2 \times N(H_2)}{N(photons)} \times 100\%$$

where N ($H_2$) denotes the quantity of $H_2$ molecules generated, and N(photons) represents the number of photons that reach the surface of the reaction suspension.

**Photoelectrochemical characterization**

The electrochemical measurements were conducted using an electrochemical workstation, model CHI 760. The experiment employed a three-electrode system, where a Pt sheet served as the counter electrode, an Ag/AgCl electrode as the reference electrode, and the prepared powder sample as the working electrode. A 0.2 M $Na_2SO_4$ solution was used as the electrolyte, and a xenon lamp with a filter ($\lambda \geq 420$ nm) provided the visible light source. To prepare the working electrode, 5 mg of the catalyst sample and 20 μL of Nafion solution were dissolved in 1 mL of anhydrous ethanol, sonicated for 30 minutes to ensure thorough mixing, and then applied onto FTO glass (1 cm × 1 cm).

1. The band gap energy of the sample can be obtained using the following formula Eq. S1:

$$\alpha h\nu = A(h\nu - E_g)^{n/2} \quad \text{(S1)}$$

In this formula, the symbols α, ν, h, Eg and A correspond to the absorption coefficient, frequency of the incident light, Planck's constant, band gap energy, and a proportionality constant, respectively.

2. The Mott-Schottky test is used to determine the band structure, and the flat band potential can be calculated using the following equation Eq. S2:

$$\frac{1}{C^2} = \frac{2}{A^2 e \varepsilon_r \varepsilon_0 N_d}\left(V - V_{fb} - \frac{kT}{e}\right) \quad \text{(S2)}$$

In this equation, C is the capacitance, A is the effective surface area, $\varepsilon_r$ and $\varepsilon_0$ are the dielectric constants of the catalyst and vacuum, respectively, e is the elementary charge, $N_d$ is the carrier concentration in the catalyst, V is the applied potential, $V_{fb}$ is the flat band potential, k is the Boltzmann constant, and T represents the absolute temperature.

3. Time-resolved photoluminescence (TRPL) spectroscopy was employed to study the separation and dynamic behavior of photogenerated charges (at a wavelength of 326 nm). The following equation Eq. S3 was used to obtain the fluorescence decay curve:

$$\tau_{av}=(A_1\cdot\tau_1^2+A_2\cdot\tau_2^2)/(A_1\cdot\tau_1+A_2\cdot\tau_2) \quad (S3)$$

where $\tau_1$ and $\tau_2$ represent the decay times, and A1 and A2 represent the PL intensities, respectively.

4. Temperature-dependent fluorescence intensity measurements were conducted at various temperatures ranging from 115 to 265 K. The following equation Eq. S4 was used to calculate the exciton binding energy:

$$I(T)=\frac{I_0}{1+Ae^{-E_b/K_BT}} \quad (S4)$$

where $I_0$ is the intensity at 0 K, $E_b$ is the binding energy, A is a proportionality constant, and $k_B$ is the Boltzmann constant.

**DFT calculations**

All calculations in this study were performed using the GGA-PBE functional, with the system charge set according to actual conditions to maintain non-polarized spin polarization. The electronic energy cutoff was set to 310 eV, the pseudopotentials were ultrasoft, and relativistic treatment was conducted using the Koelling-Harmon approach. The SCF tolerance was set to $2\times10^{-6}$ eV/atom. The binding energy EE between substances and the free energy of hydrogen production GG were calculated as follows equation Eq. S5 and S6:

$$\mathrm{E} = E_{ab} - E_a - E_b \tag{S5}$$

The total energy of the system after binding is $E_{ab}$, and $E_a$ and $E_b$ are the energies of the two components before binding, respectively.

$$\mathrm{G} = G_{H*} - G_* - G_{(\frac{1}{2})H2} \tag{S6}$$

Where $G_{H*}$ is the free energy of the system when forming a hydrogen radical, $G_*$ and $G_{(\frac{1}{2})H2}$ are the free energies of the clean surface and half a hydrogen molecule, respectively.[1-3]

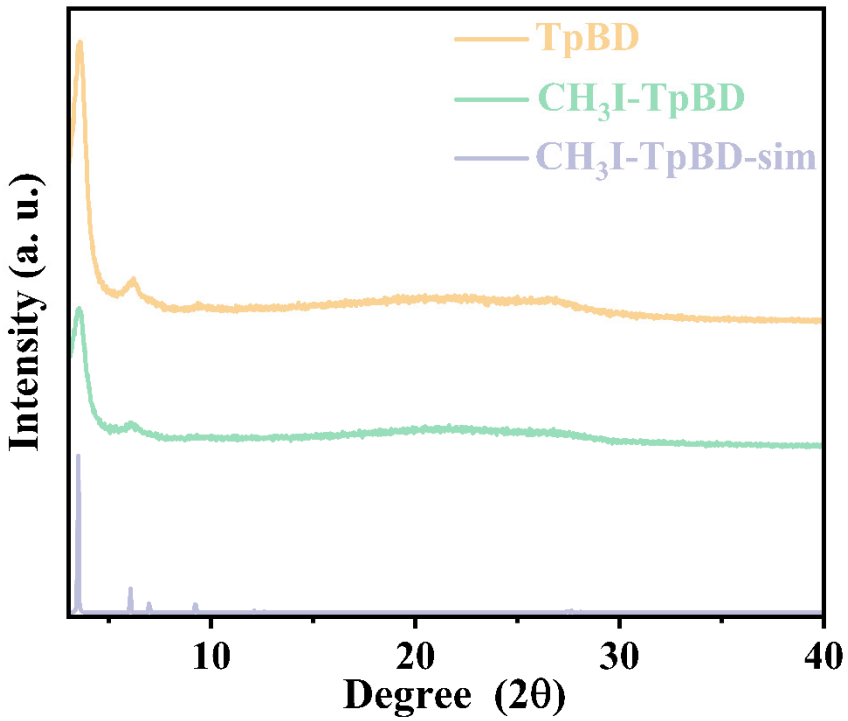


**Fig. S1**: Powder X-ray diffraction patterns of TpBD, $CH_3I$-TpBD and simulated TpBD.

**Note:** The diffraction peak positions of TpBD and $CH_3I$-TpBD can match well with the simulated standard card, proving the successful synthesis of TpBD and $CH_3I$-TpBD.

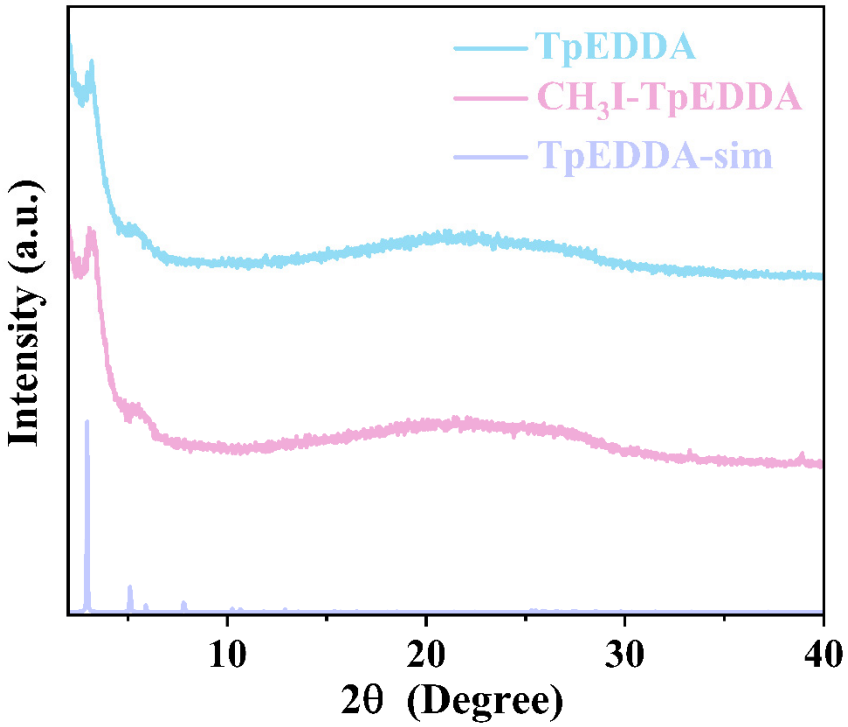


**Fig. S2:** Powder X-ray diffraction patterns of TpEDDA, $CH_3I$-TpEDDA and simulated TpEDDA.

**Note:** The diffraction peak positions of TpEDDA and $CH_3I$-TpEDDA can match well with the simulated standard card, proving the successful synthesis of TpEDDA and $CH_3I$-TpEDDA.

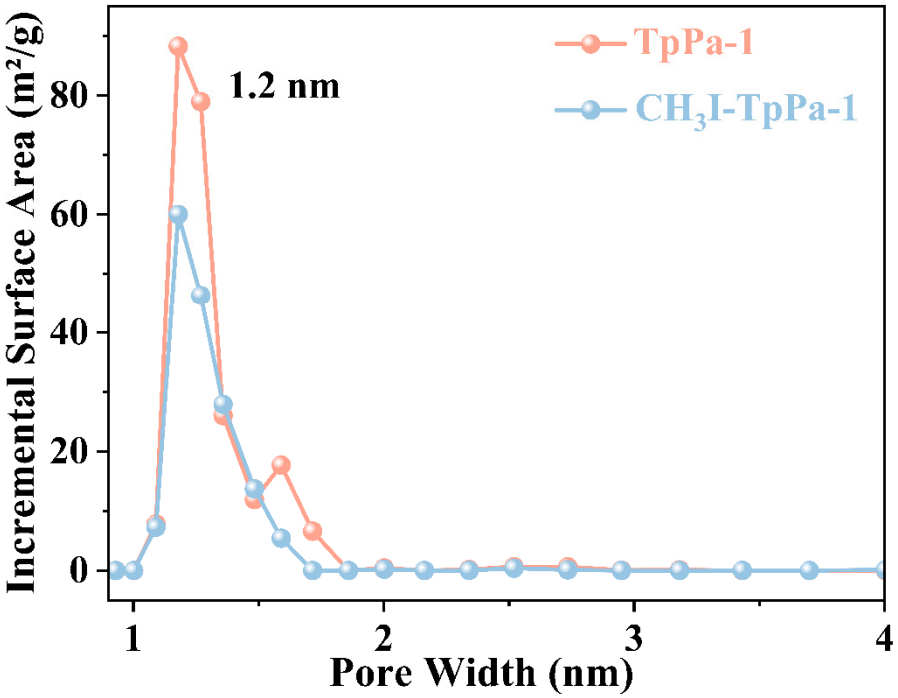


**Fig. S3:** Pore size distribution plots of TpPa-1 and $CH_3I$-TpPa-1.

**Note:** The pore diameter of TpPa-1 and $CH_3I$-TpPa-1 is approximately 1.2 nm.

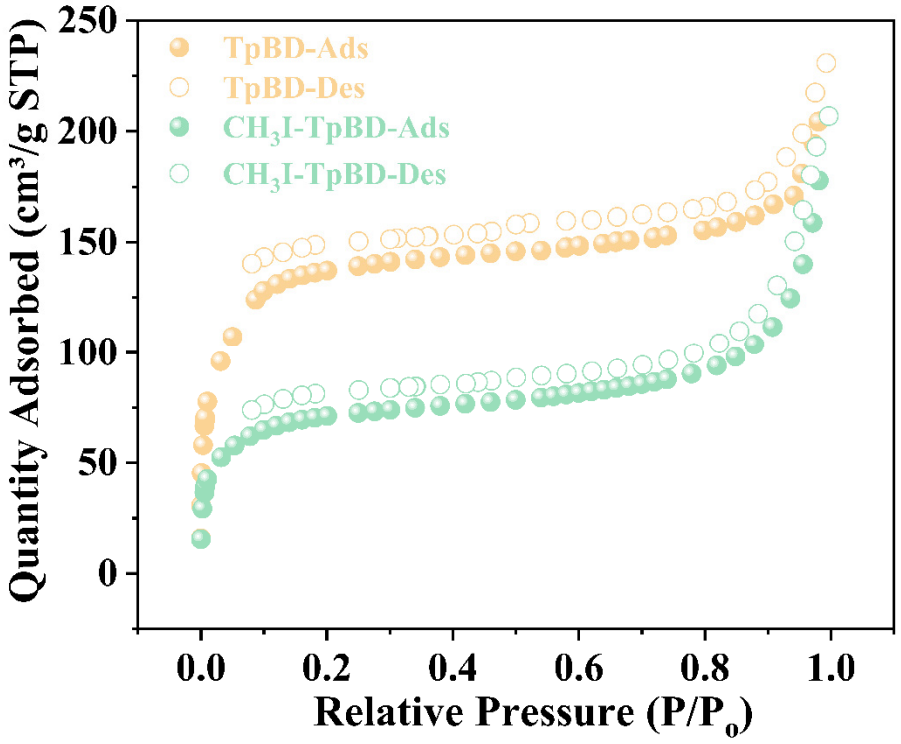


**Fig. S4:** $N_2$ adsorption–desorption isotherms of TpBD and $CH_3I$-TpBD.

**Note:** $N_2$ adsorption/desorption isotherms were analyzed for the prepared samples, demonstrated that both TpBD and $CH_3I$-TpBD displayed a type I isotherm, characterized by a steep slope and strong adsorption capacity at low pressure, indicating the presence of typical micropores within their structures.

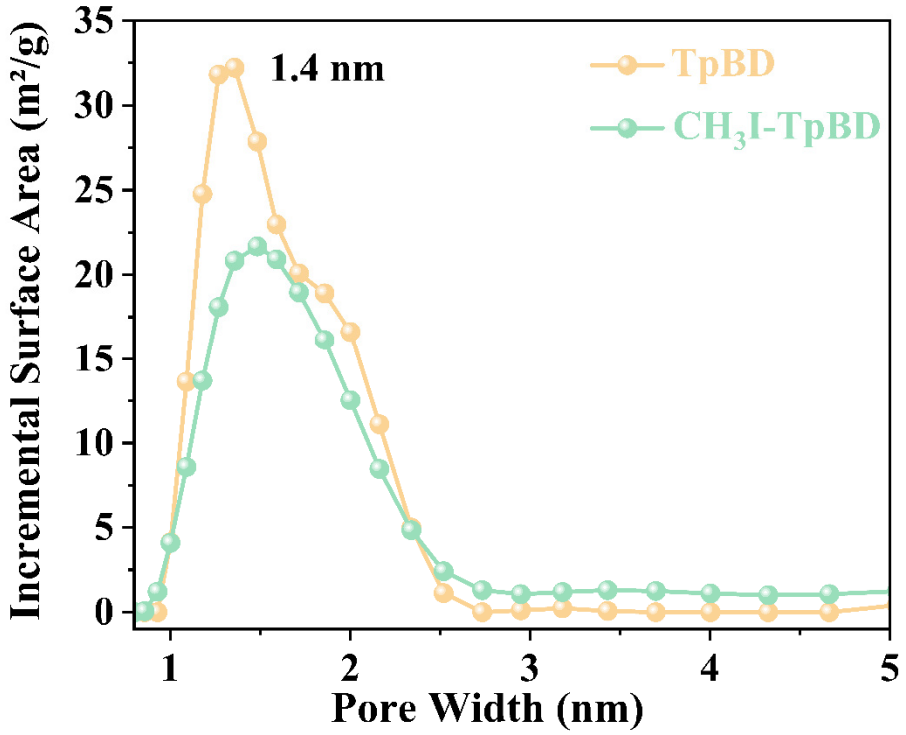


**Fig. S5:** Pore size distribution plots of TpBD and $CH_3I$-TpBD.

**Note:** The pore diameter of TpBD and $CH_3I$-TpBD is approximately 1.4 nm.

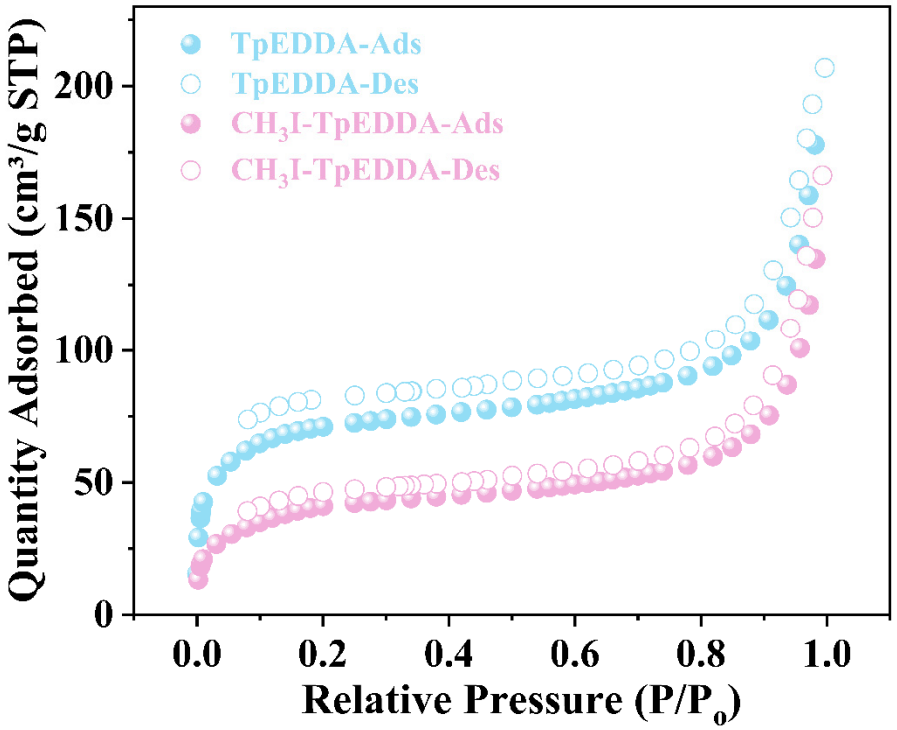


**Fig. S6:** $N_2$ adsorption–desorption isotherms of TpEDDA and $CH_3I$-TpEDDA.

**Note:** $N_2$ adsorption/desorption isotherms were analyzed for the prepared samples, demonstrated that both TpEDDA and $CH_3I$-TpEDDA displayed a type I isotherm, characterized by a steep slope and strong adsorption capacity at low pressure, indicating the presence of typical micropores within their structures.

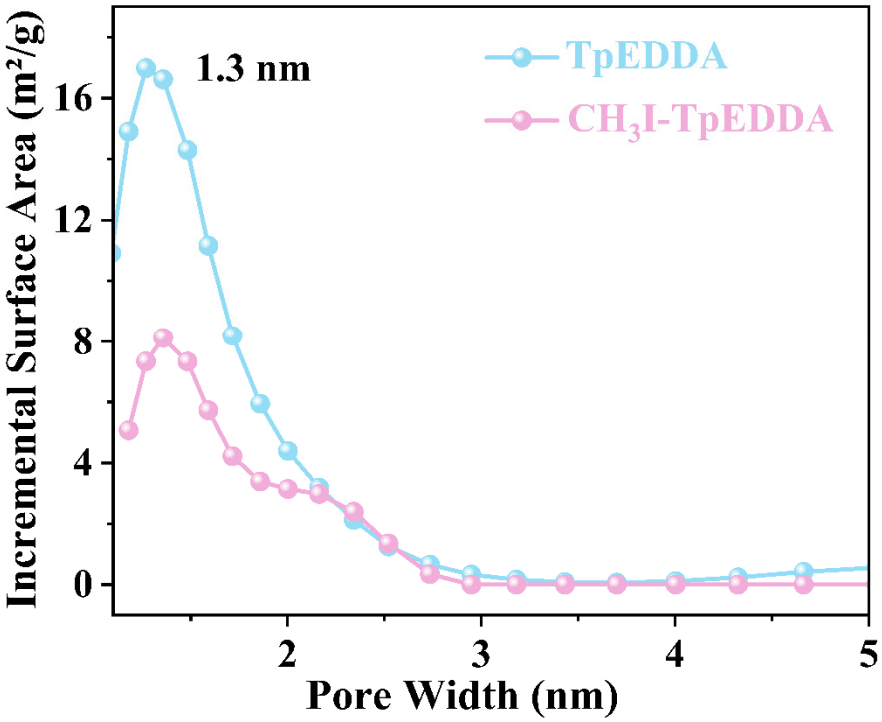


**Fig. S7**: Pore size distribution plots of TpEDDA and $CH_3I$-TpEDDA.

**Note:** The pore diameter of TpEDDA and $CH_3I$-TpEDDA. is approximately 1.3 nm.

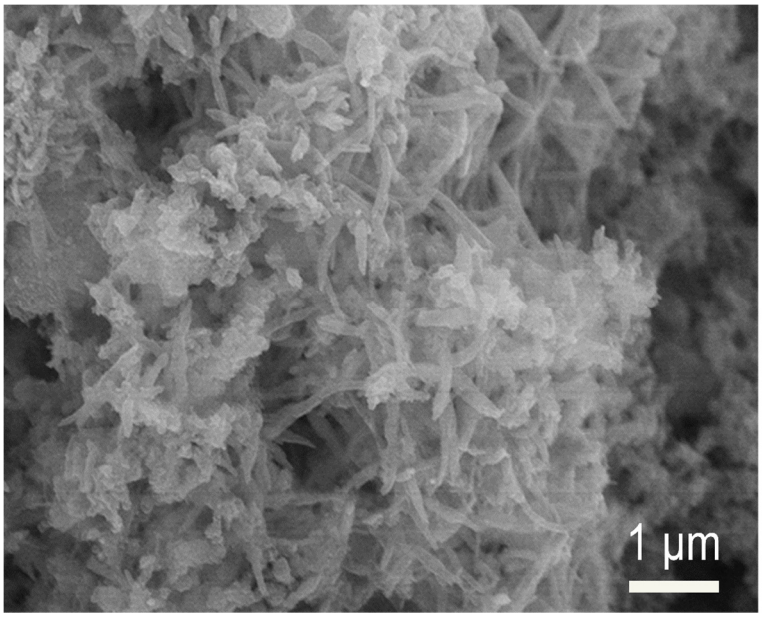


**Fig. S8** SEM image of TpPa-1

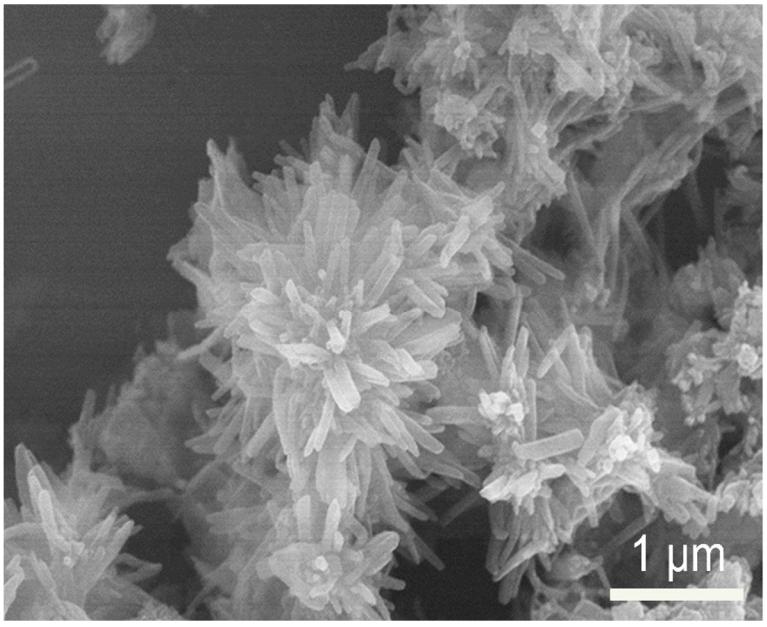


**Fig. S9** SEM image of $CH_3I$-TpPa-1

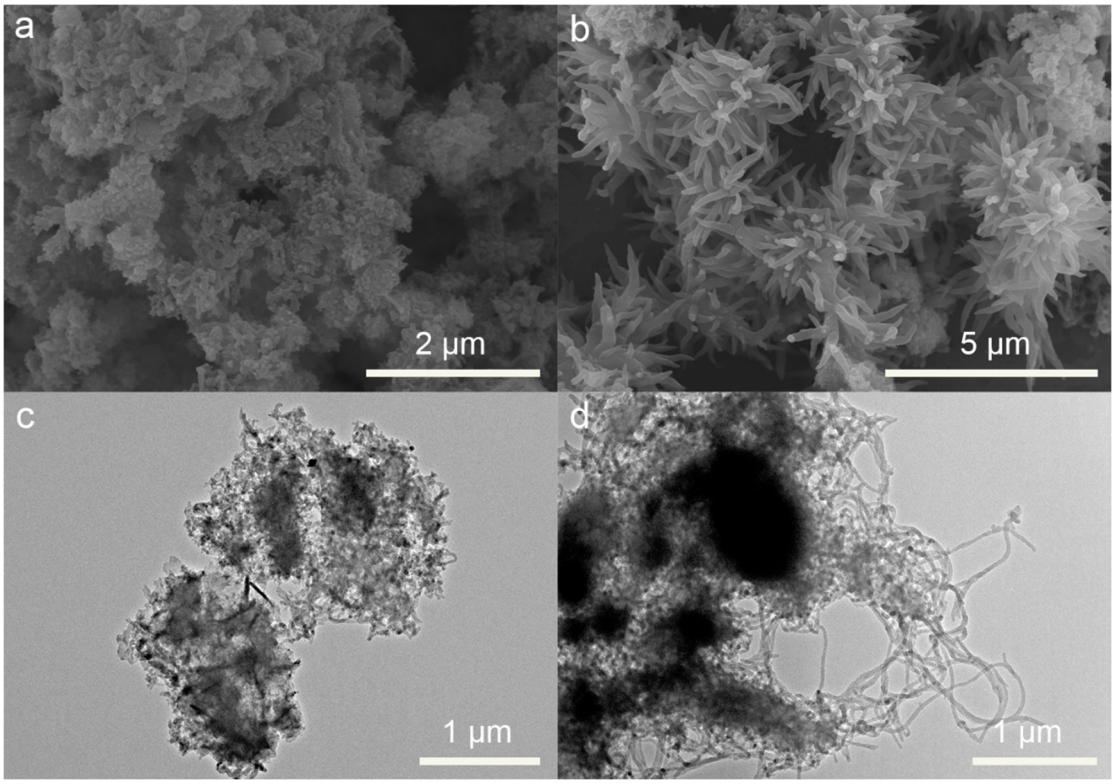


**Fig. S10**: **a, b** SEM images of TpBD and $CH_3I$-TpBD. **c, d** TEM images of TpBD and $CH_3I$-TpBD.

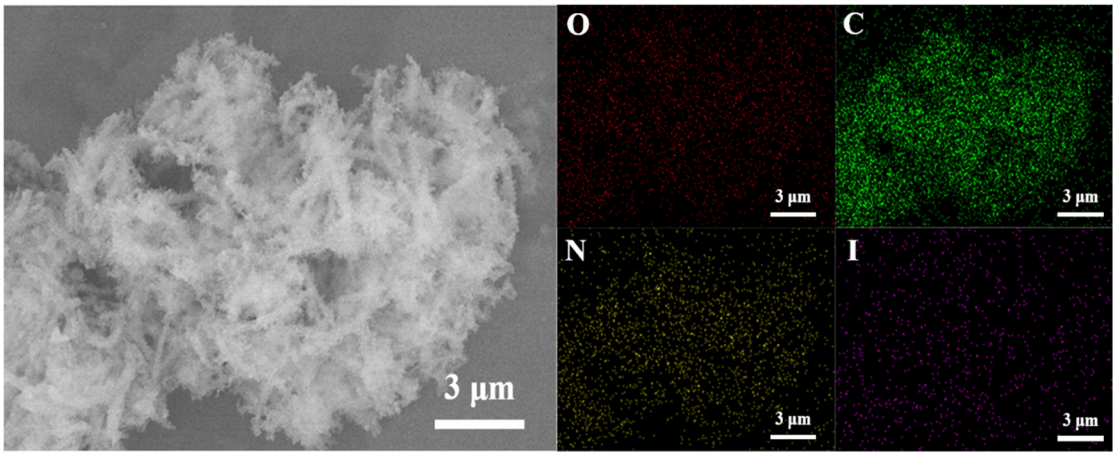


**Fig. S11:** SEM elemental maps of $CH_3I$-TpBD.

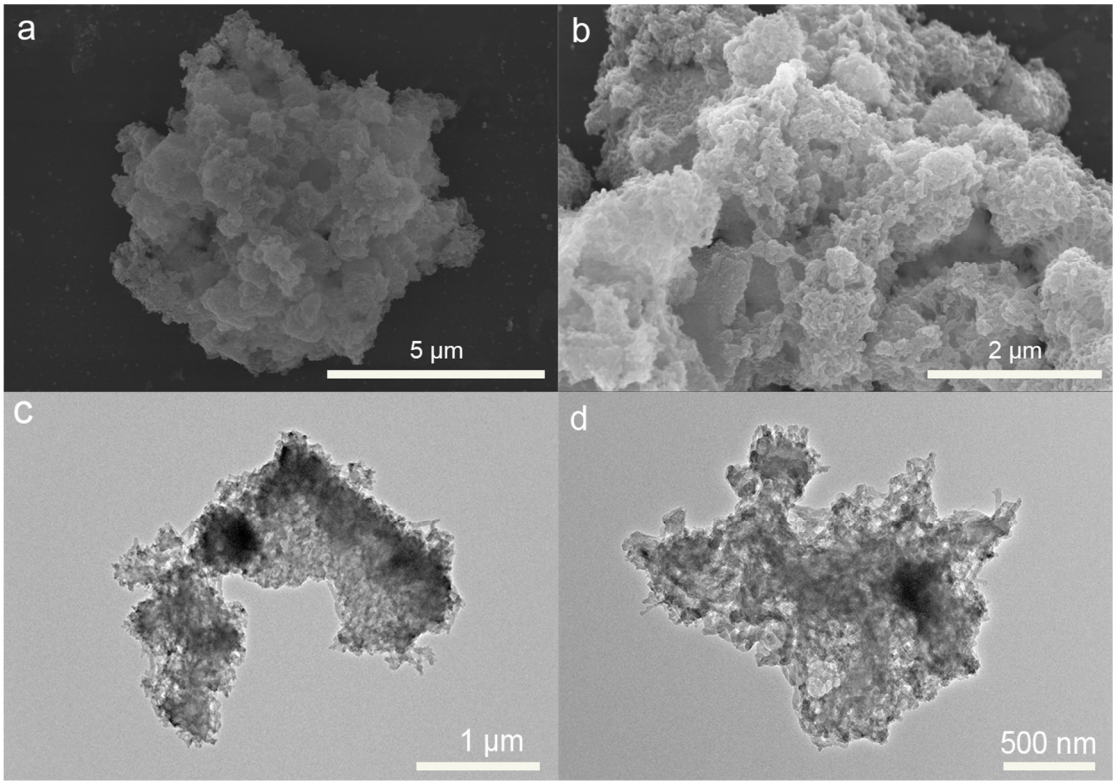


**Fig. S12: a, b** SEM images of TpEEDA and $CH_3I$-TpEDDA. **c, d** TEM images of TpEDDA and $CH_3I$-TpEDDA.

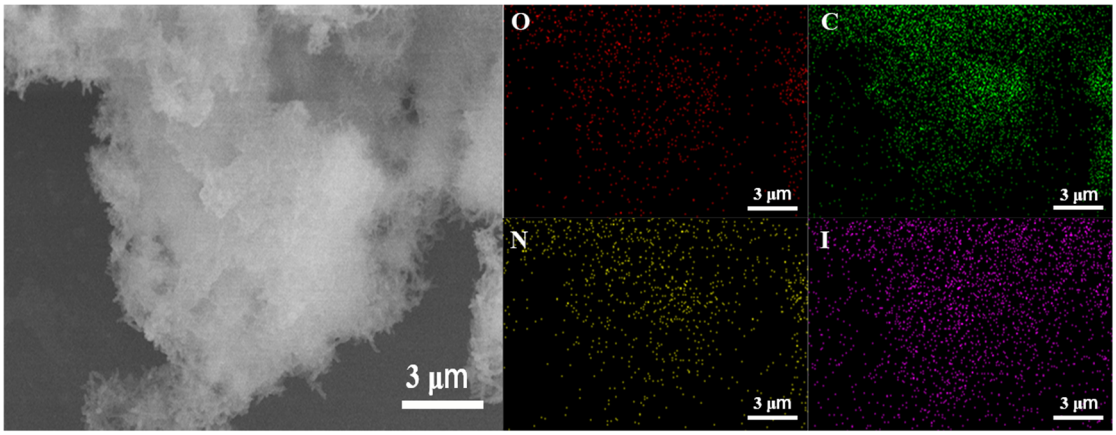


**Fig. S13:** SEM elemental maps of $CH_3I$-TpEDDA.

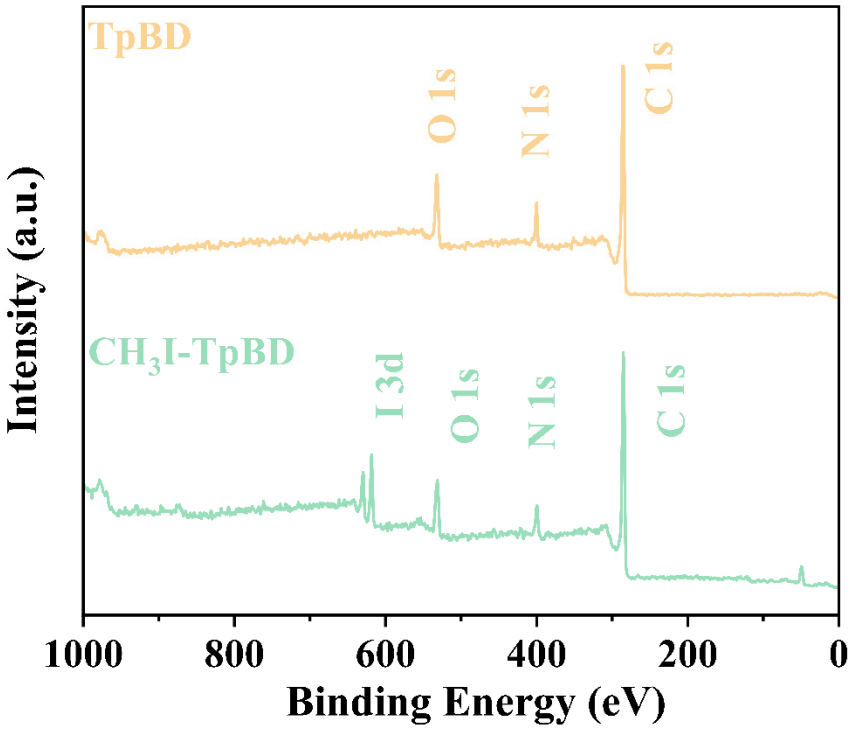


**Fig. S14:** The survey XPS spectra of TpBD and $CH_3I$-TpBD.

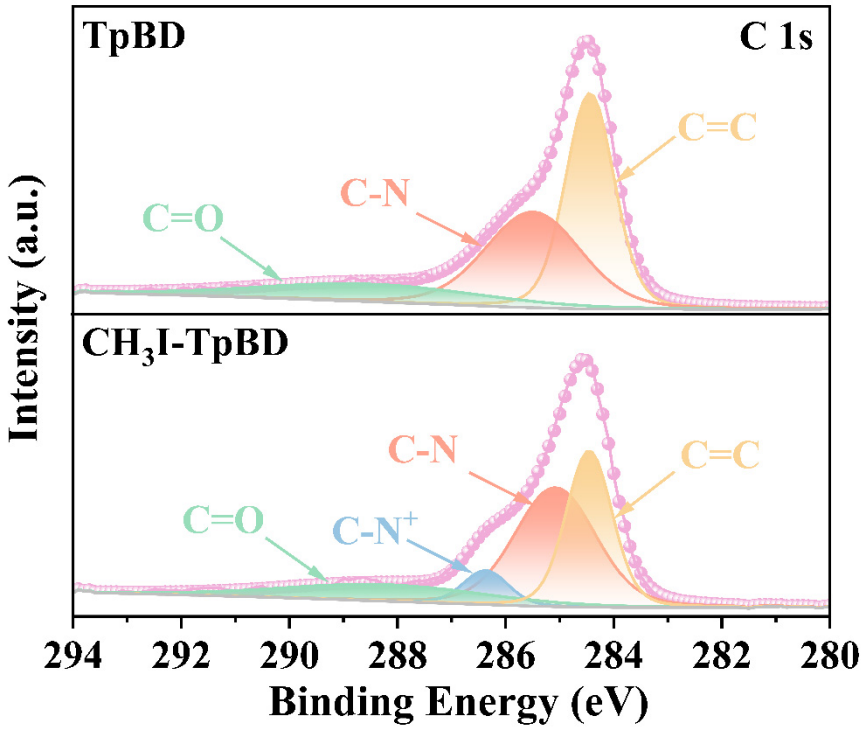


**Fig. S15:** C 1s High-resolution XPS spectra of TpBD and $CH_3I$-TpBD.

**Note:** The high-resolution C 1s spectrum of TpBD was clearly shown in Figure S15, where the peaks of binding energies at 284.4 eV, 285.4 eV, and 288.9 eV corresponded to the C=C, C-N, and C=O groups, respectively. The high-resolution C 1s spectrum of $CH_3I$-TpBD was clearly shown in Figure S15, where the peaks of binding energies at 284.4 eV, 285.1 eV, 288.6 eV and 286.4 eV corresponded to the C=C, C-N, C=O and C-$N^+$ groups, respectively.

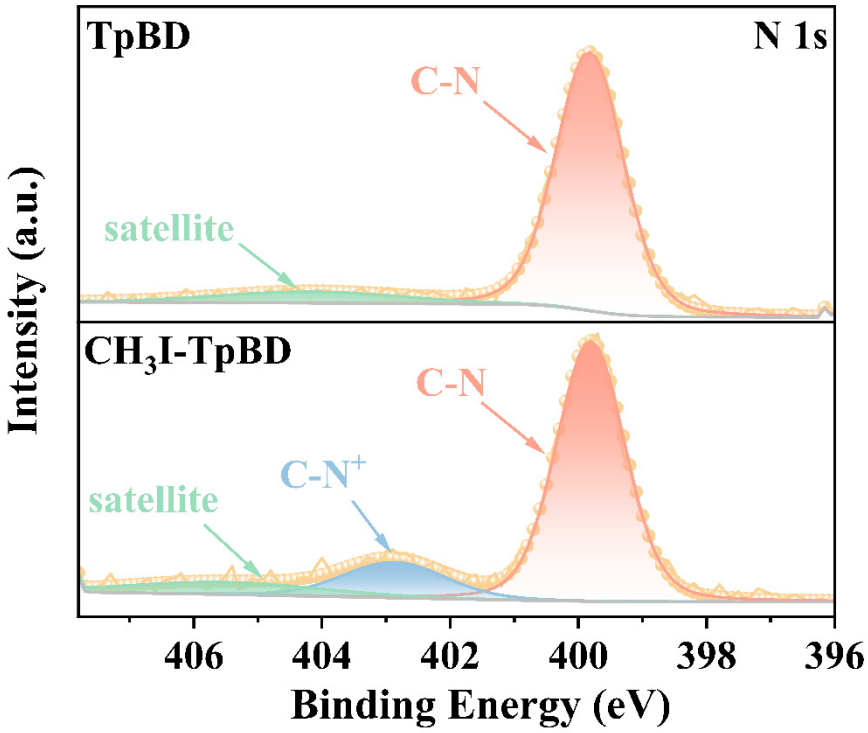


**Fig. S16:** N 1s High-resolution XPS spectra of TpBD and $CH_3I$-TpBD.

**Note:** As depicted in Figure S16, the high-resolution N 1s spectrum of bare TpBD can be distinguished by two peaks at 399.8 eV and 404.1 eV, where the peak at 404.1 eV is identified as a satellite peak. The high-resolution N 1s spectrum of bare $CH_3I$-TpBD can be distinguished by two peaks at 399.8 eV ,403.3 and 406.5 eV, where the peak at 406.5 eV is identified as a satellite peak.

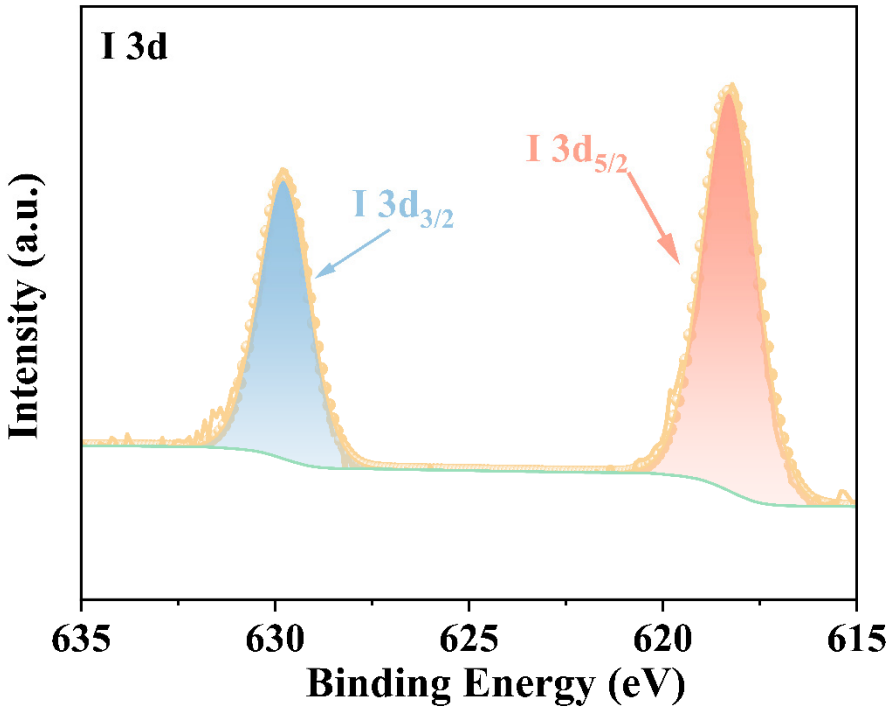


**Fig. S17:** I 3d High-resolution XPS spectra of $CH_3I$-TpBD.

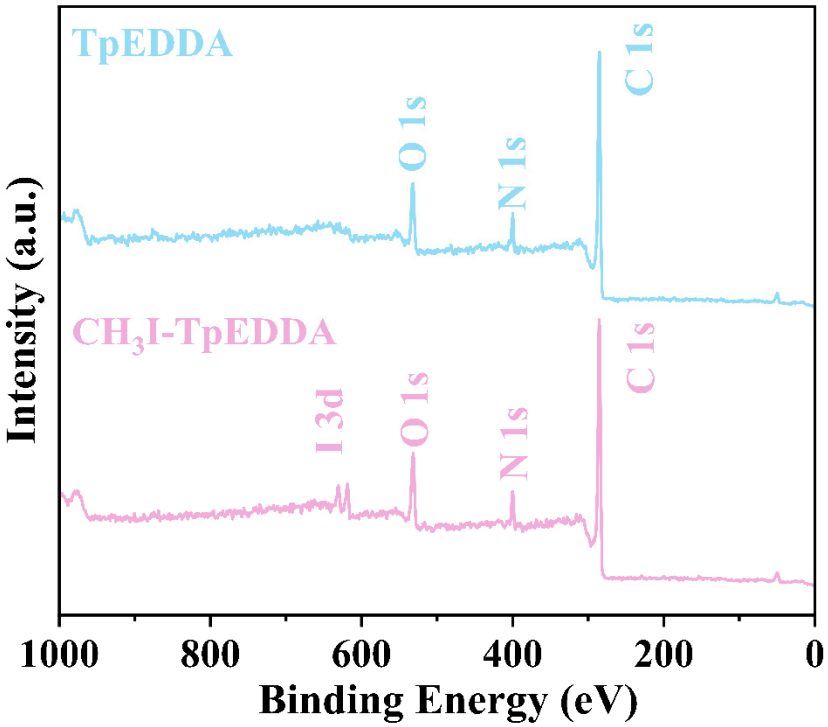


**Fig. S18:** The survey XPS spectra of TpEDDA and $CH_3I$-TpEDDA.

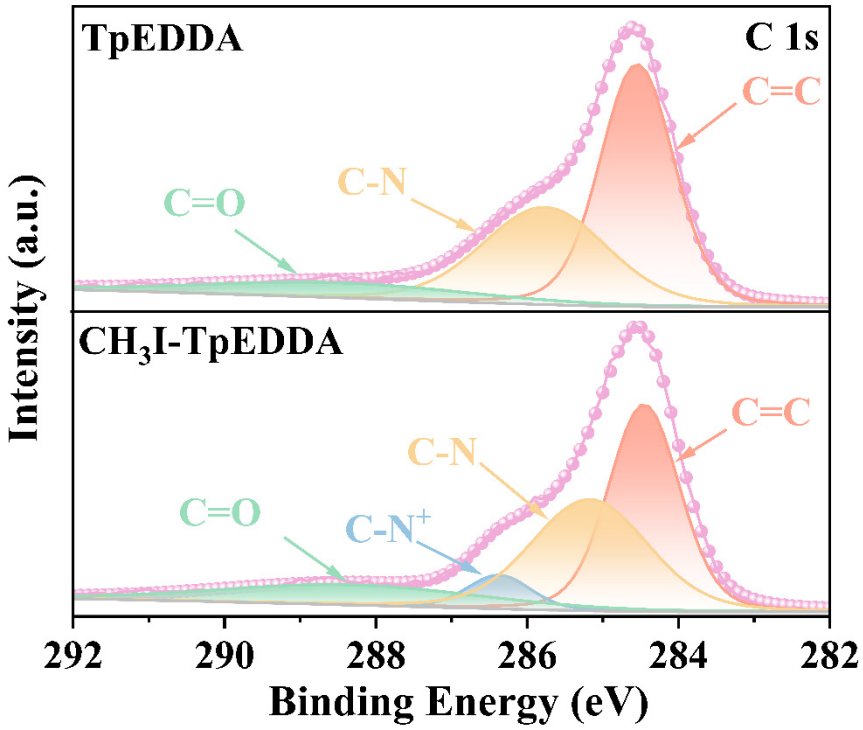


**Fig. S19:** C 1s High-resolution XPS spectra of TpEDDA and $CH_3I$-TpEDDA.

**Note:** The high-resolution C 1s spectrum of TpEDDA was clearly shown in Figure S19, where the peaks of binding energies at 284.5 eV, 285.7 eV, and 289.0 eV corresponded to the C=C, C-N, and C=O groups, respectively. The high-resolution C 1s spectrum of $CH_3I$-TpEDDA was shown in Figure S19, where the peaks of binding energies at 284.5 eV, 285.2 eV, 288.6 eV and 286.4 eV corresponded to the C=C, C-N, C=O and $C\text{-}N^+$ groups, respectively.

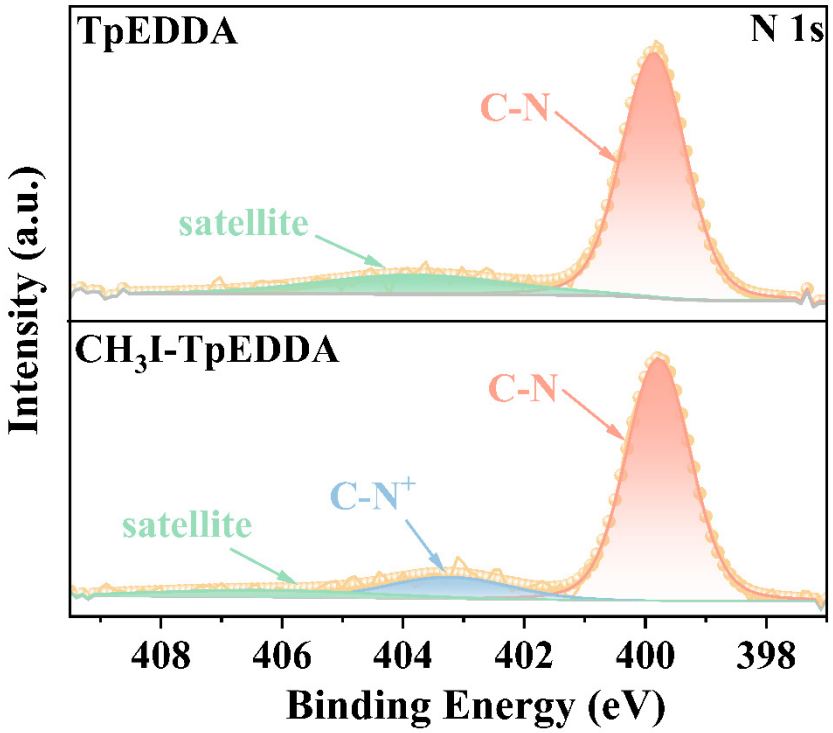


**Fig. S20:** N 1s High-resolution XPS spectra of TpEDDA and $CH_3I$-TpEDDA.

**Note:** As depicted in Figure S20, the high-resolution N 1s spectrum of bare TpEDDA can be distinguished by two peaks at 399.8 eV and 403.9 eV, where the peak at 403.9 eV is identified as a satellite peak. The high-resolution N 1s spectrum of $CH_3I$-TpEDDA can be distinguished by two peaks at 399.8 eV ,403.2 and 406.4 eV, where the peak at 406.4 eV is identified as a satellite peak.

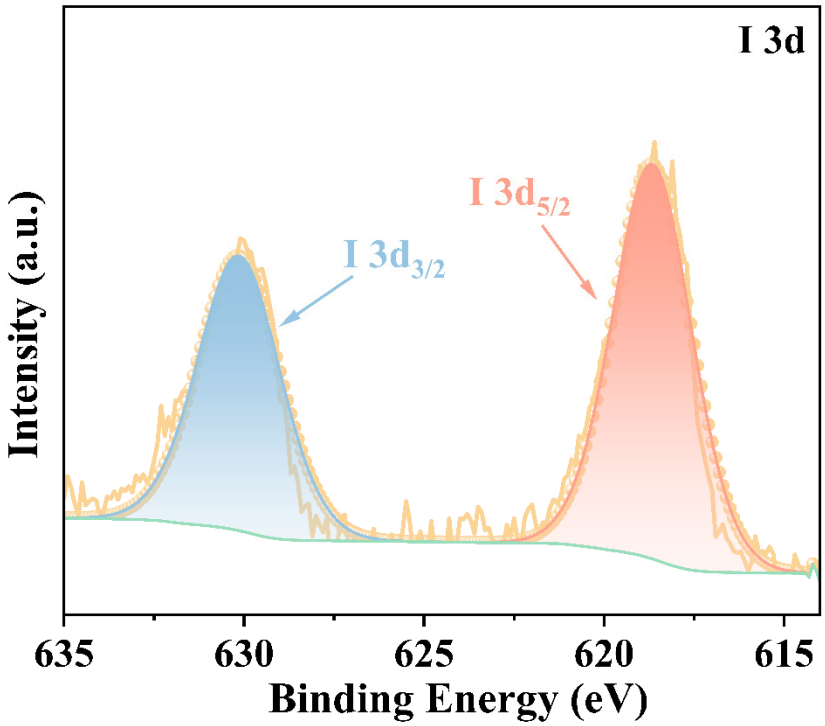


**Fig. S21:** I 3d High-resolution XPS spectra of $CH_3I$-TpEDDA.

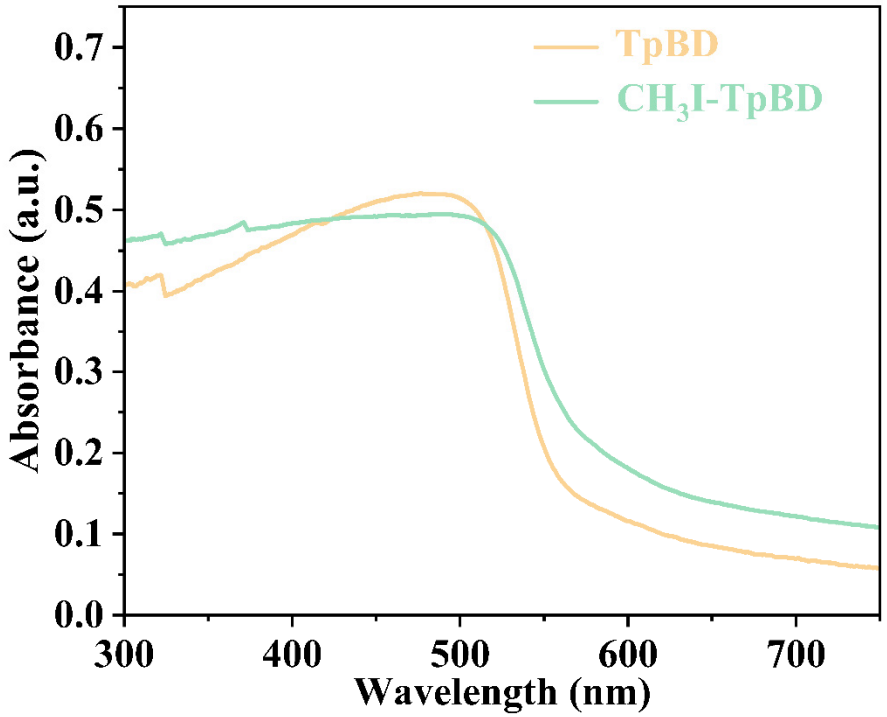


**Fig. S22:** UV–vis diffuse reflectance spectra of TpBD and $CH_3I$-TpBD.

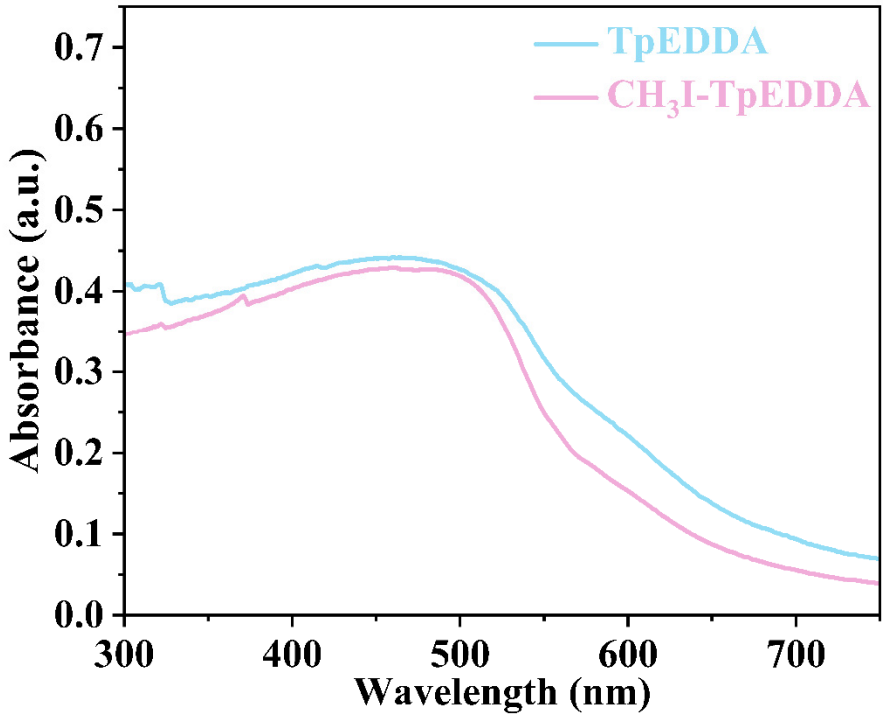


**Fig. S23:** UV–vis diffuse reflectance spectra of TpEDDA and $CH_3I$-TpEDDA.

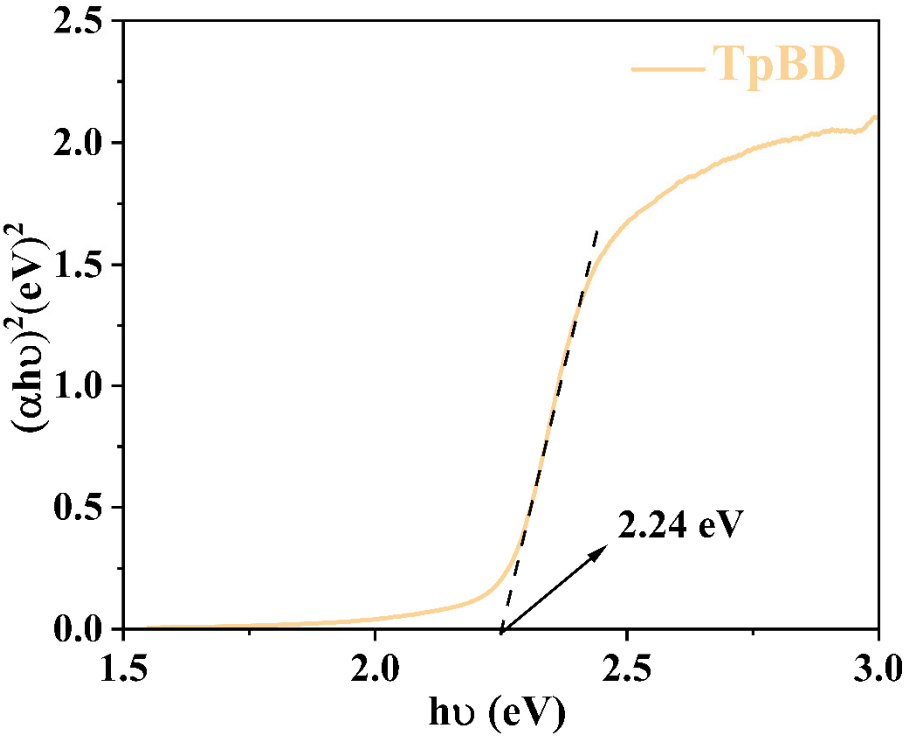


**Fig. S24:** Tauc plot of TpBD.

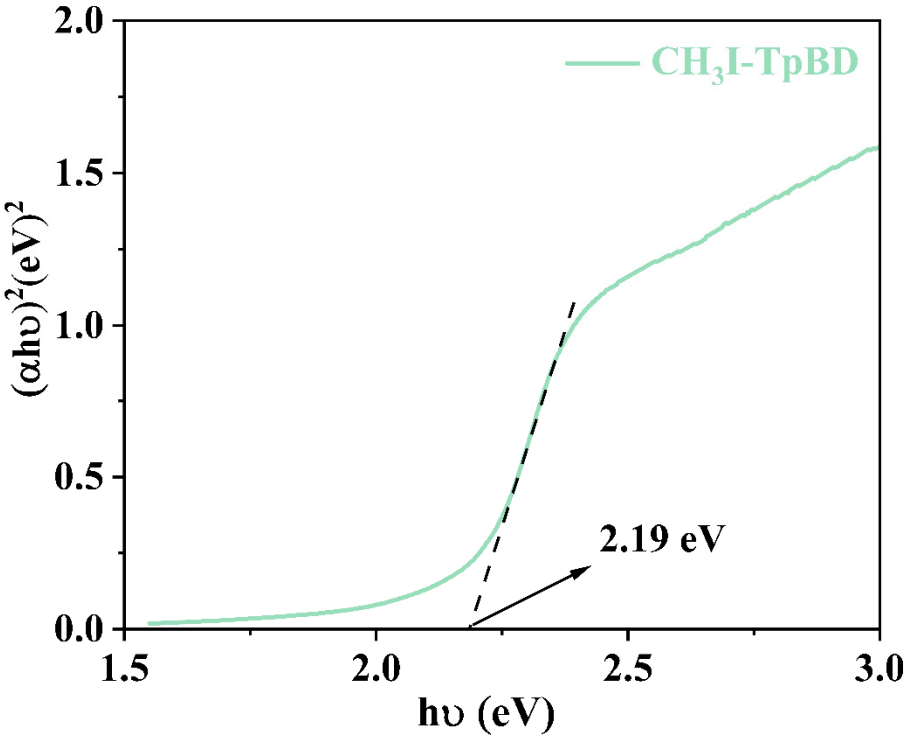


**Fig. S25:** Tauc plot of $CH_3I$-TpBD.

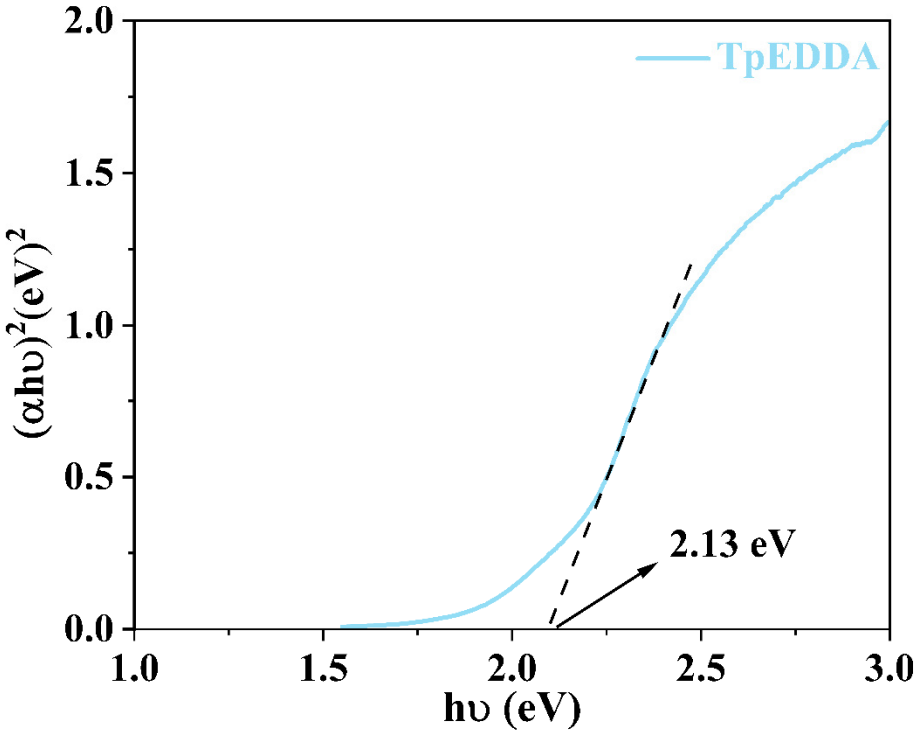


**Fig. S26:** Tauc plot of TpEDDA.

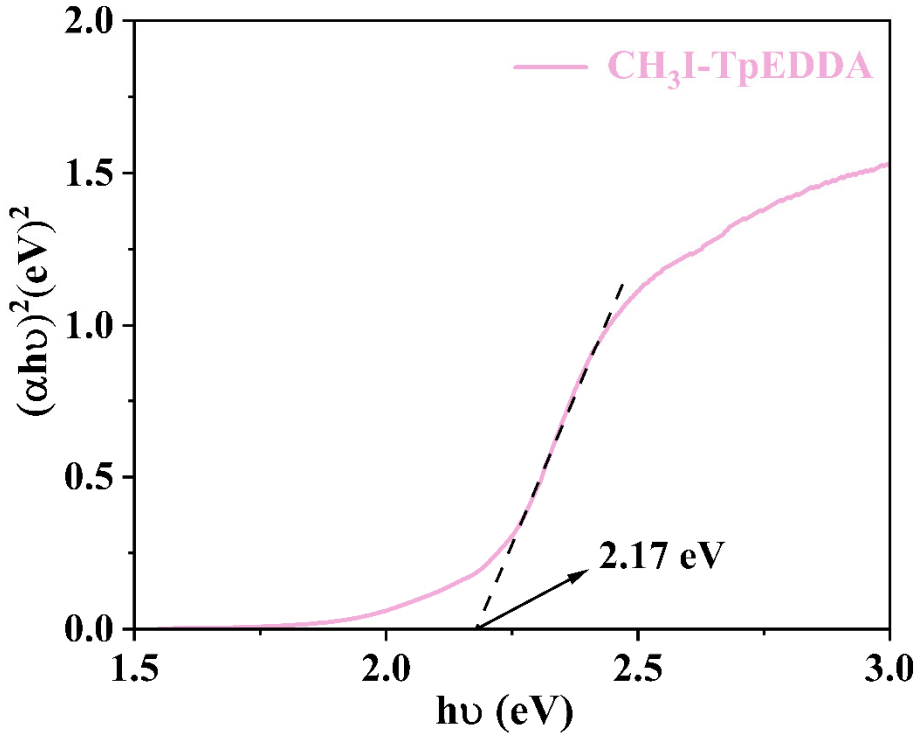


**Fig. S27:** Tauc plot of $CH_3I$-TpEDDA.

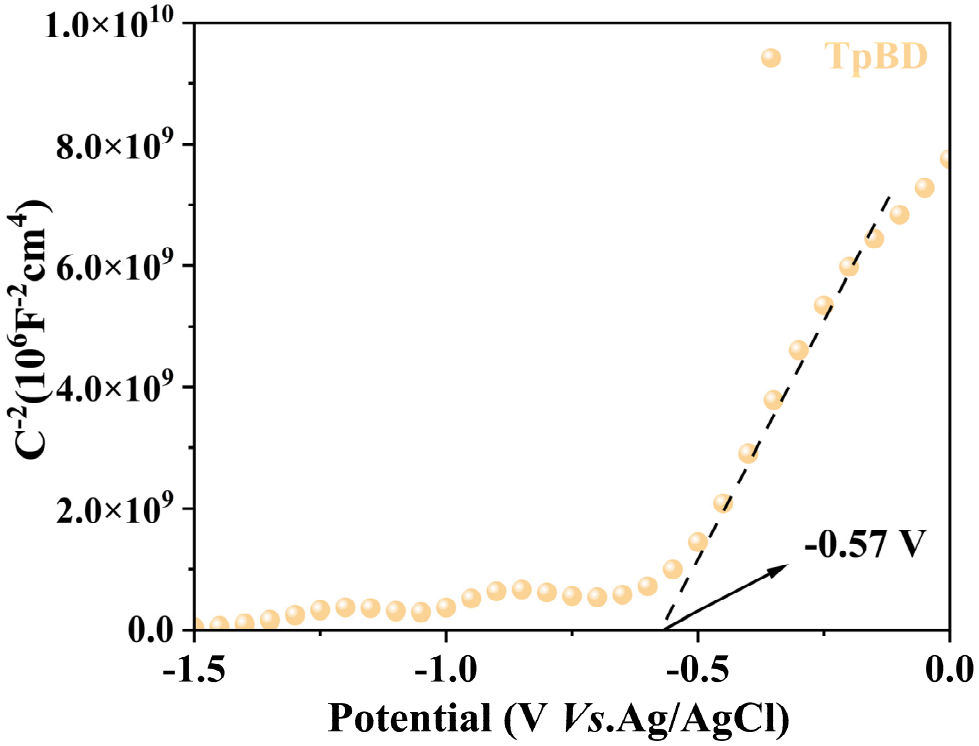


**Fig. S28:** Mott–Schottky plots of TpBD.

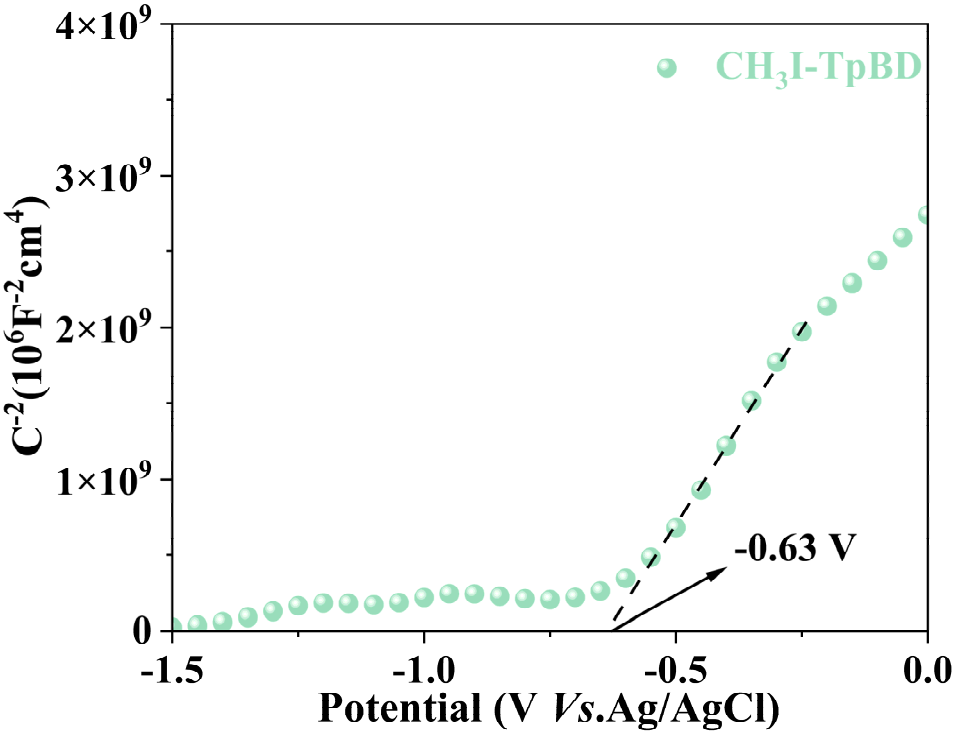


**Fig. S29:** Mott–Schottky plots of $CH_3I$-TpBD.

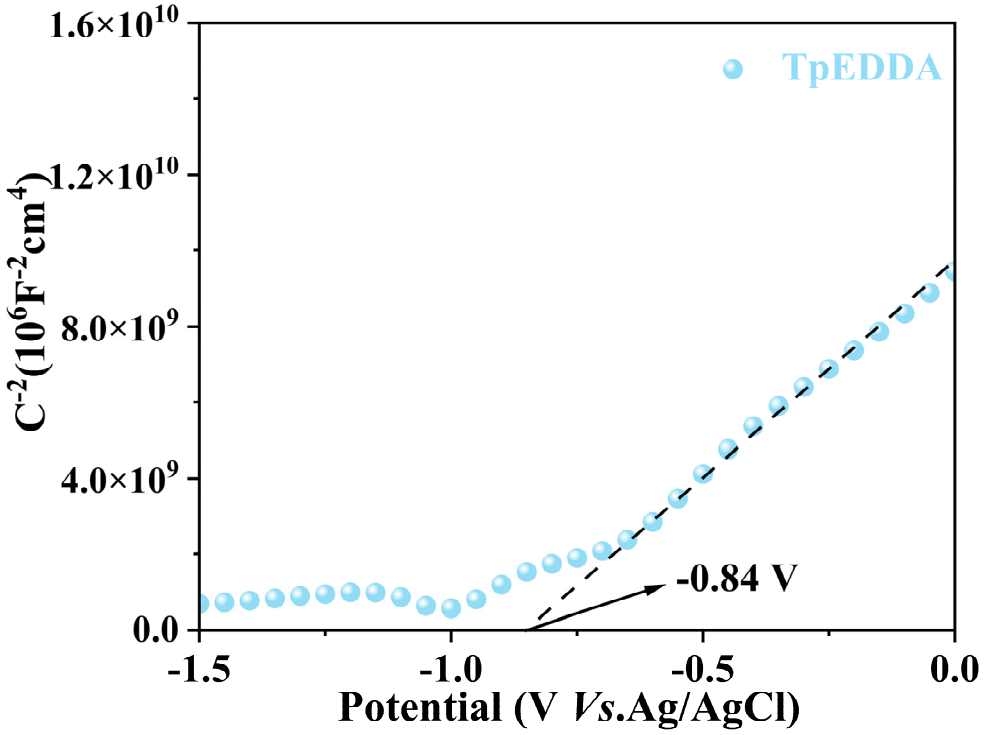


**Fig. S30:** Mott–Schottky plots of TpEDDA.

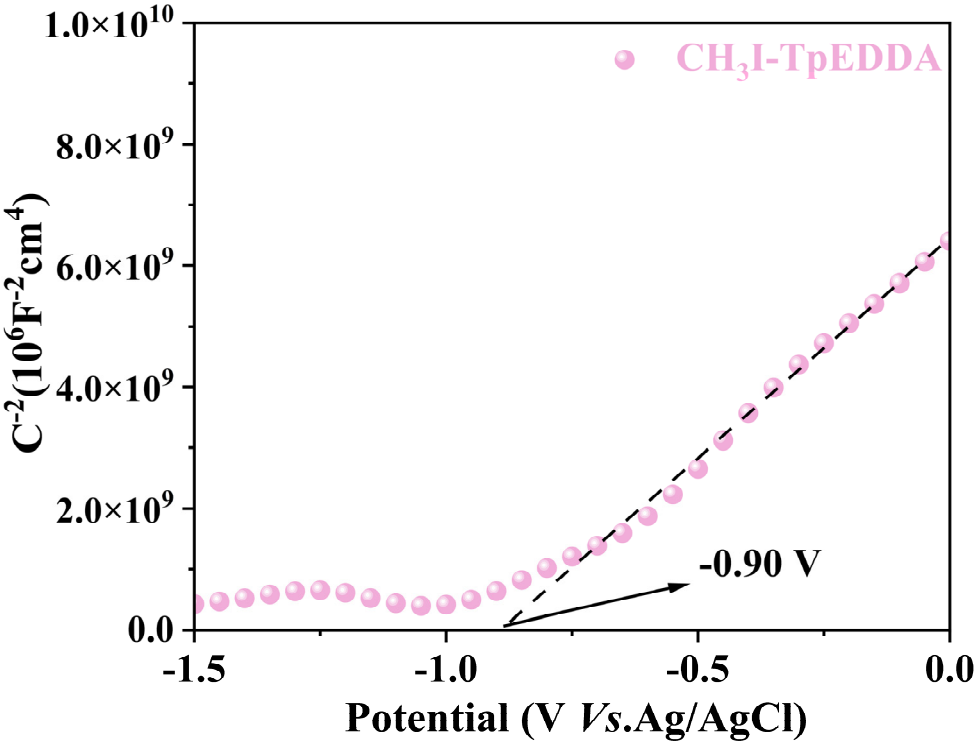


**Fig. S31:** Mott–Schottky plots of $CH_3I$-TpEDDA.

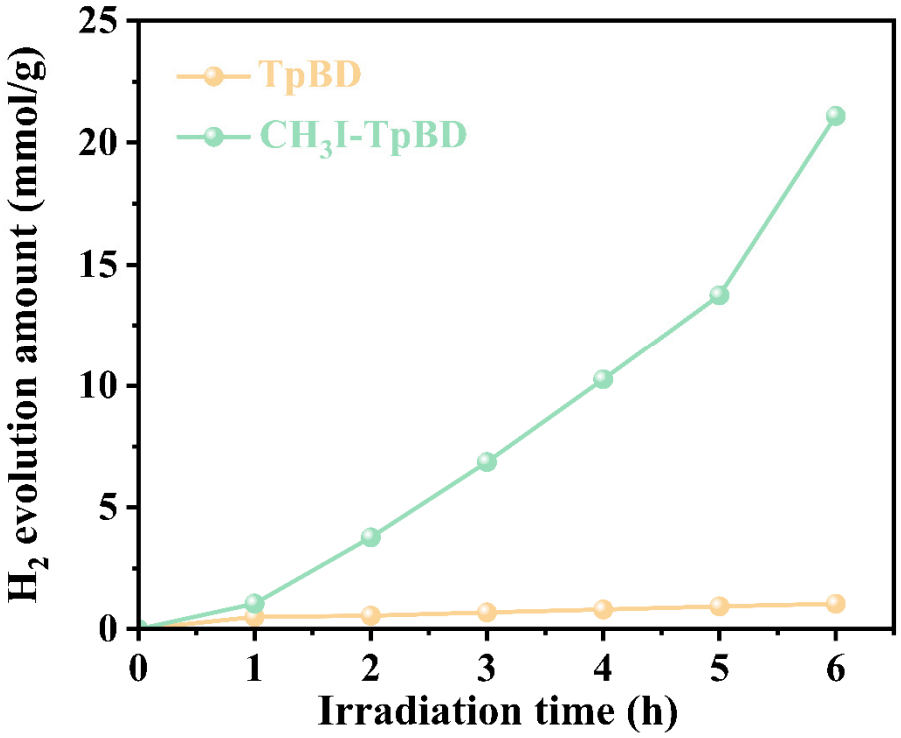


**Fig. S32:** Photocatalytic $H_2$ evolution amount comparison with time of TpBD and $CH_3I$-TpBD.

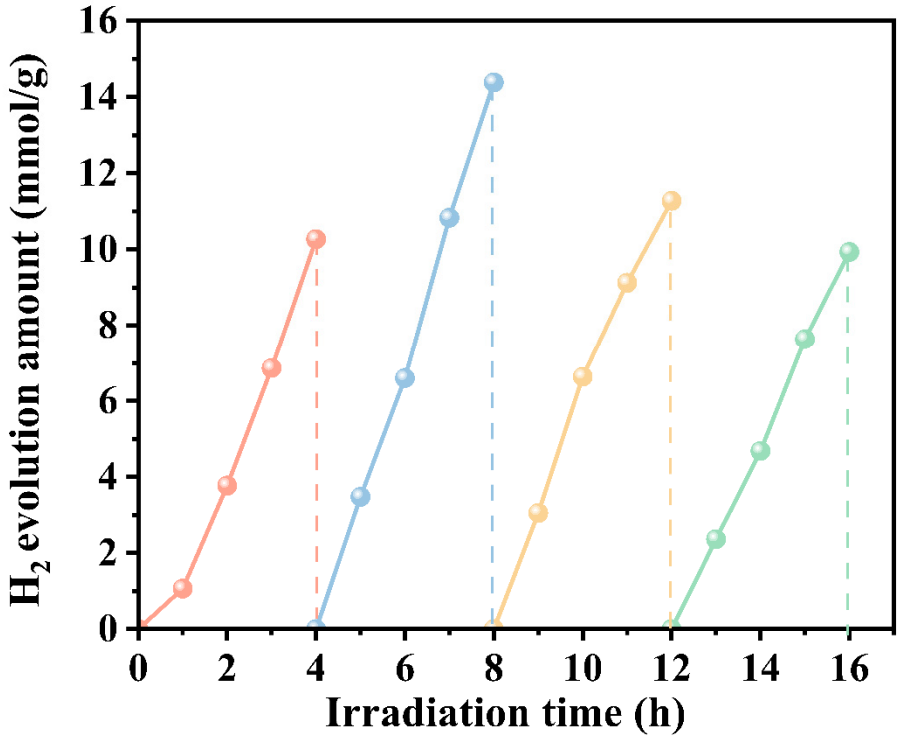


**Fig. S33:** Recycling performance of $CH_3I$-TpBD. Demonstrated the stability of $CH_3I$-TpBD in the reaction

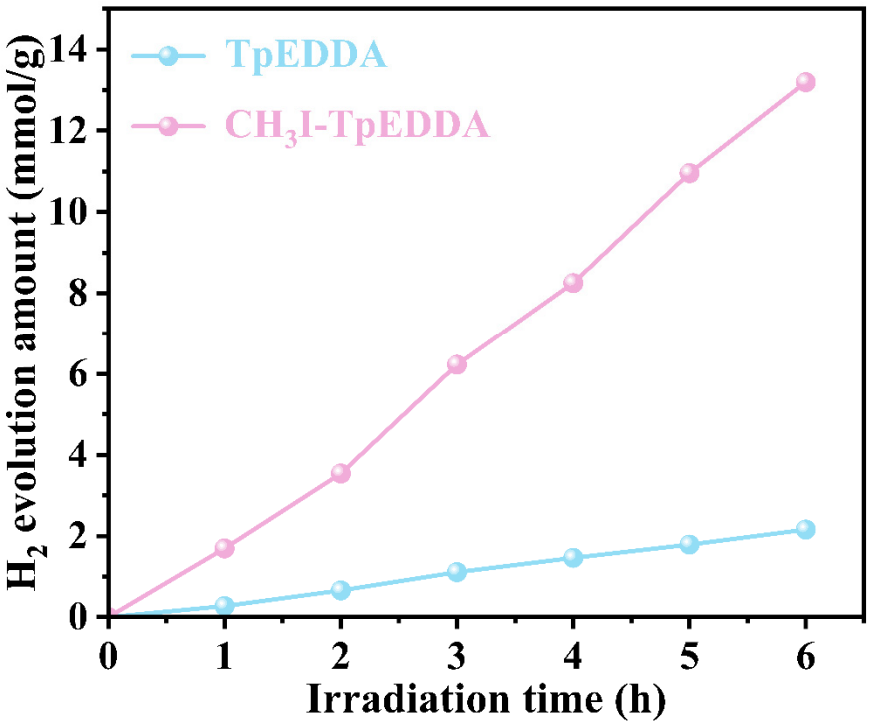


**Fig. S34:** Photocatalytic $H_2$ evolution amount comparison with time of TpEDDA and $CH_3I$-TpEDDA.

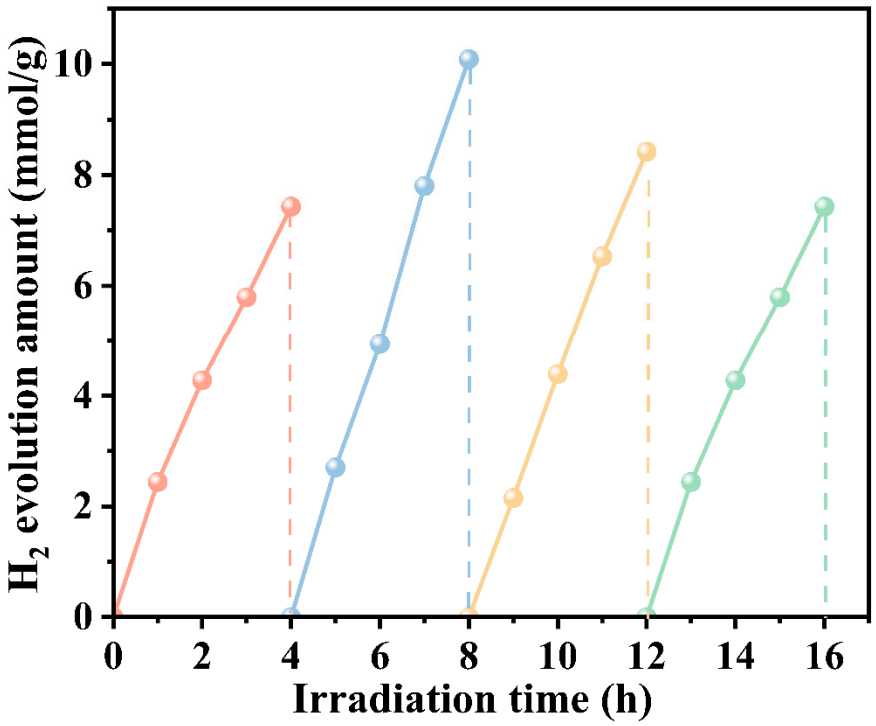


**Fig. S35:** Recycling performance of $CH_3I$-TpEDDA. Demonstrated the stability of $CH_3I$-TpEDDA in the reaction.

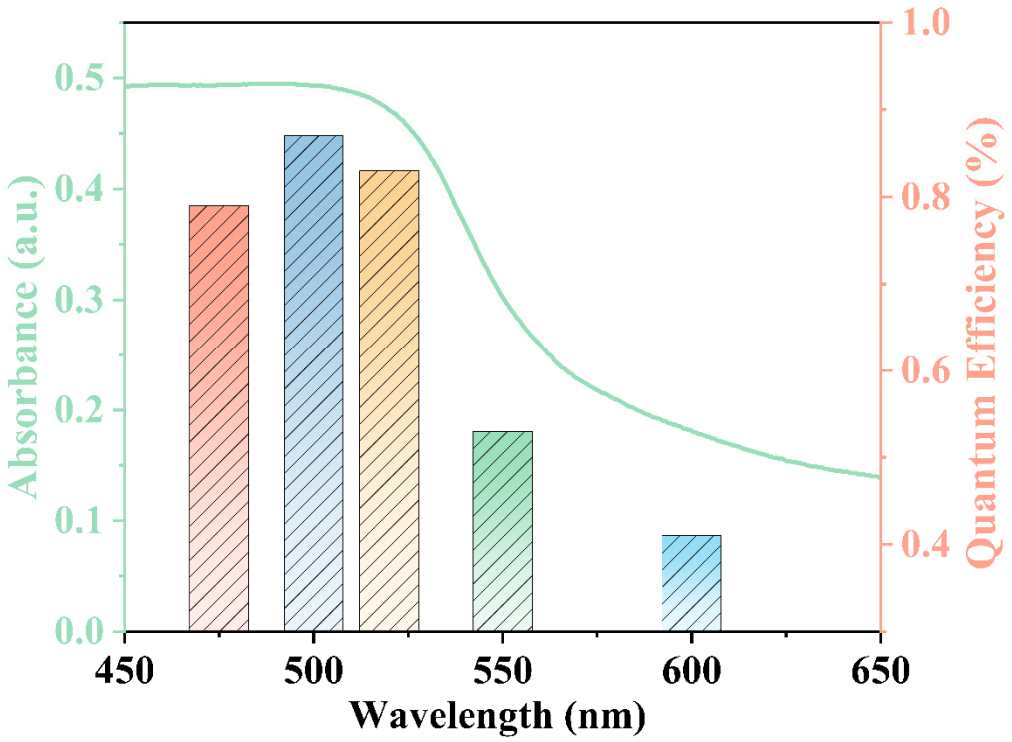


**Fig. S36:** Wavelength-dependent apparent quantum efficiency (AQE) of $CH_3I$-TpBD.

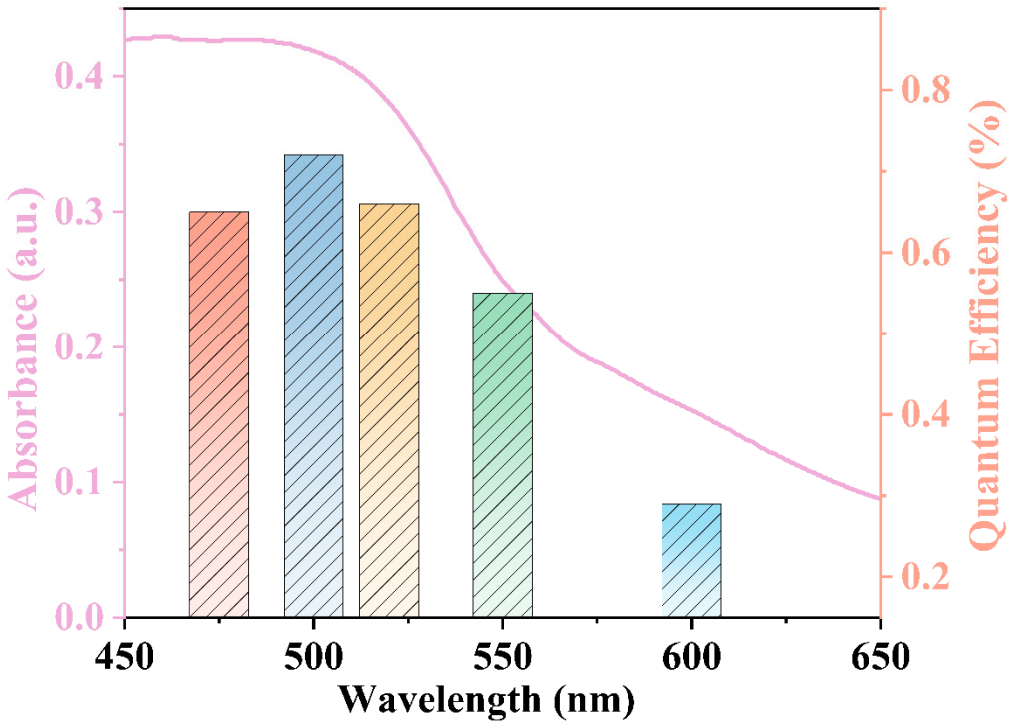


**Fig. S37:** Wavelength-dependent apparent quantum efficiency (AQE) of $CH_3I$-TpEDDA.

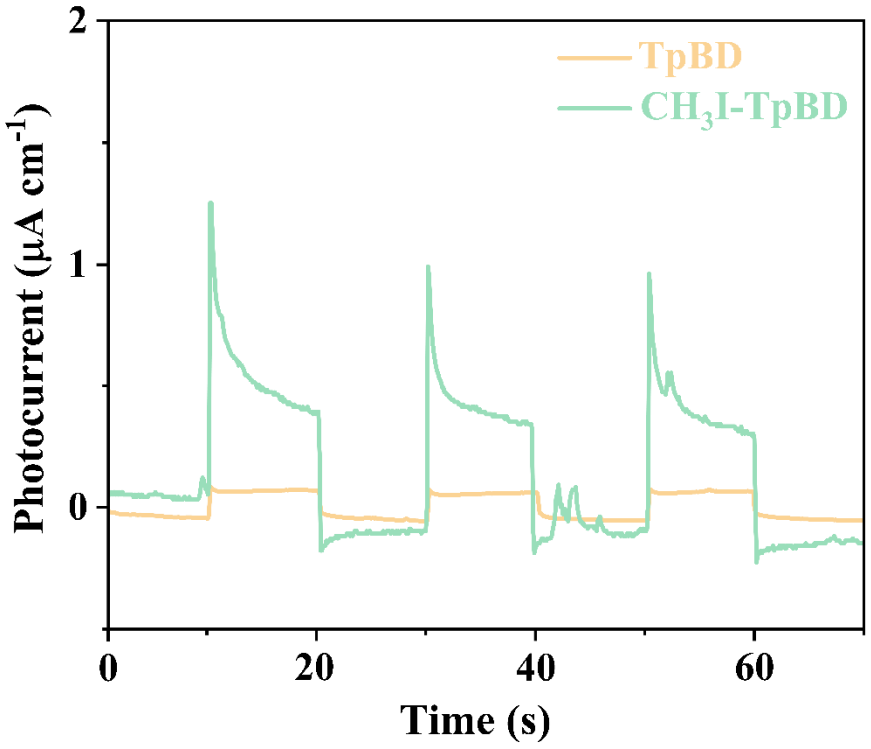


**Fig. S38:** Transient photocurrent response of TpBD and $CH_3I$-TpBD.

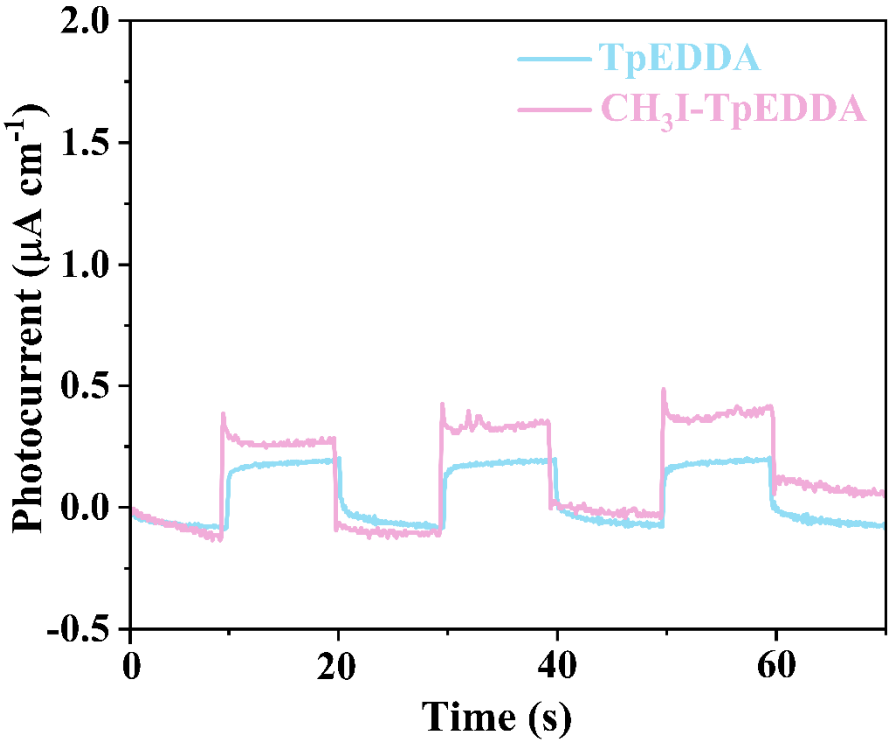


**Fig. S39:** Transient photocurrent response of TpEDDA and $CH_3I$-TpEDDA.

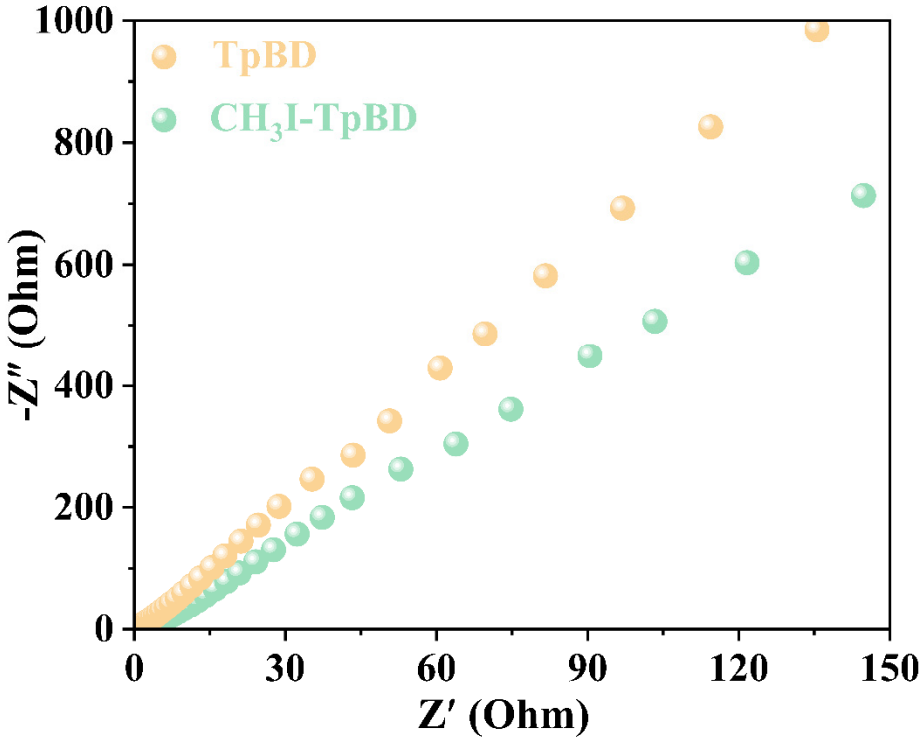


**Fig. S40:** EIS Nyquist plots of TpBD and $CH_3I$-TpBD.

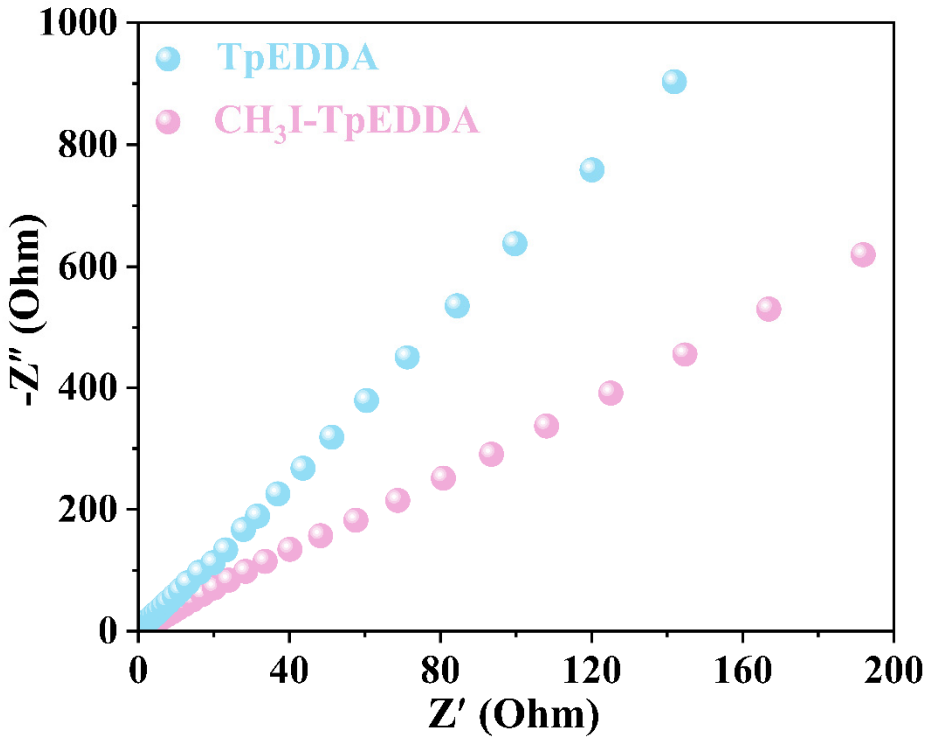


**Fig. S41:** EIS Nyquist plots of TpEDDA and $CH_3I$-TpEDDA.

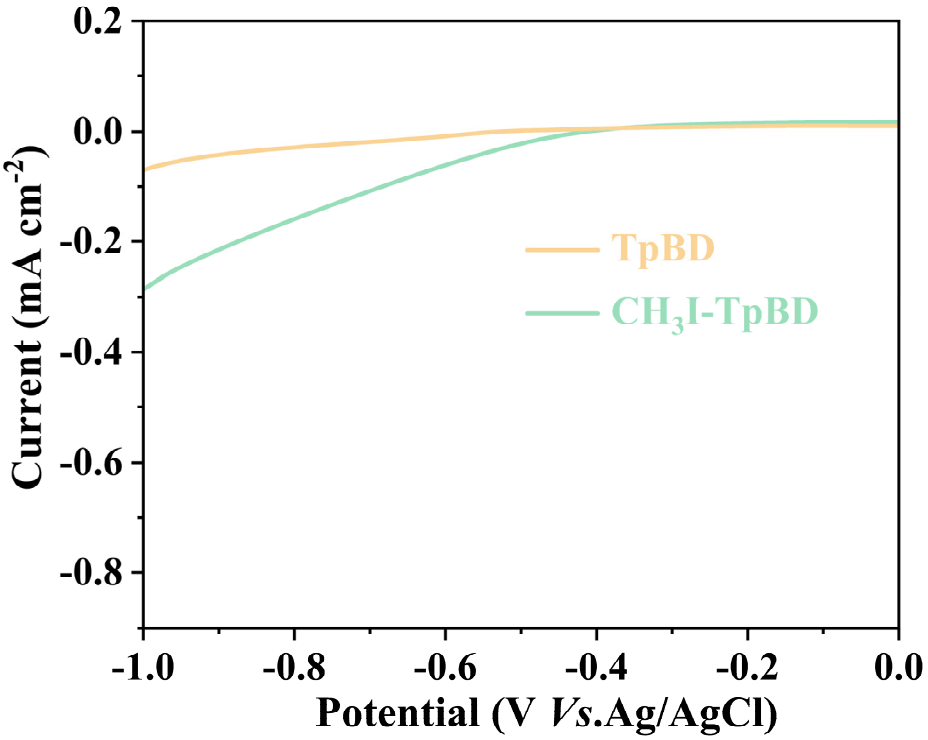


**Fig. S42:** LSV curves of TpBD and $CH_3I$-TpBD.

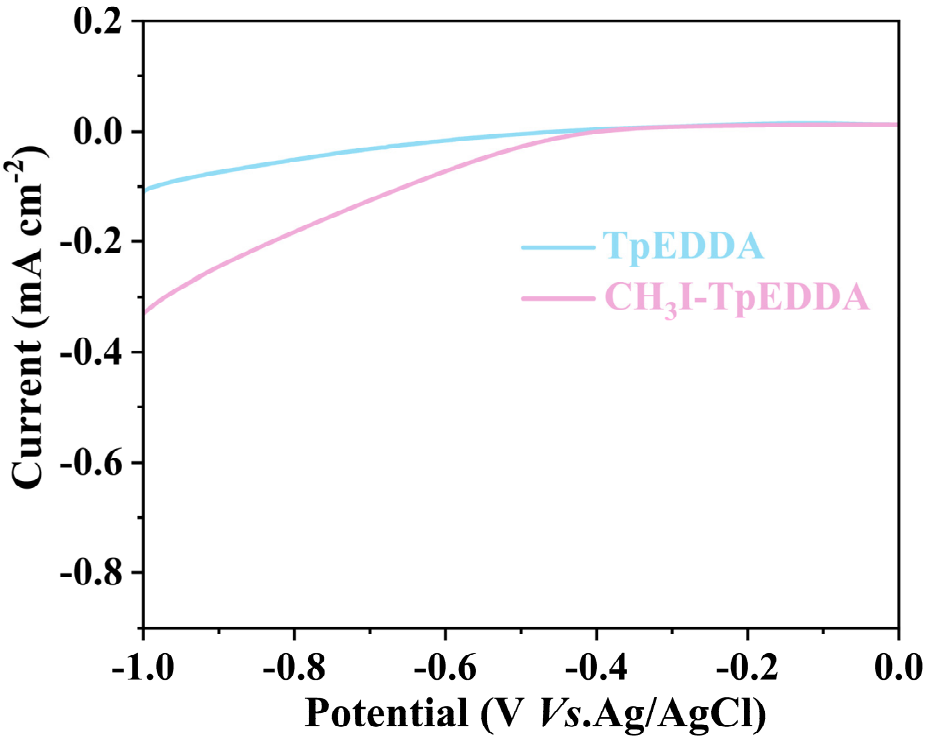


**Fig. S43:** LSV curves of TpEDDA and $CH_3I$-TpEDDA.

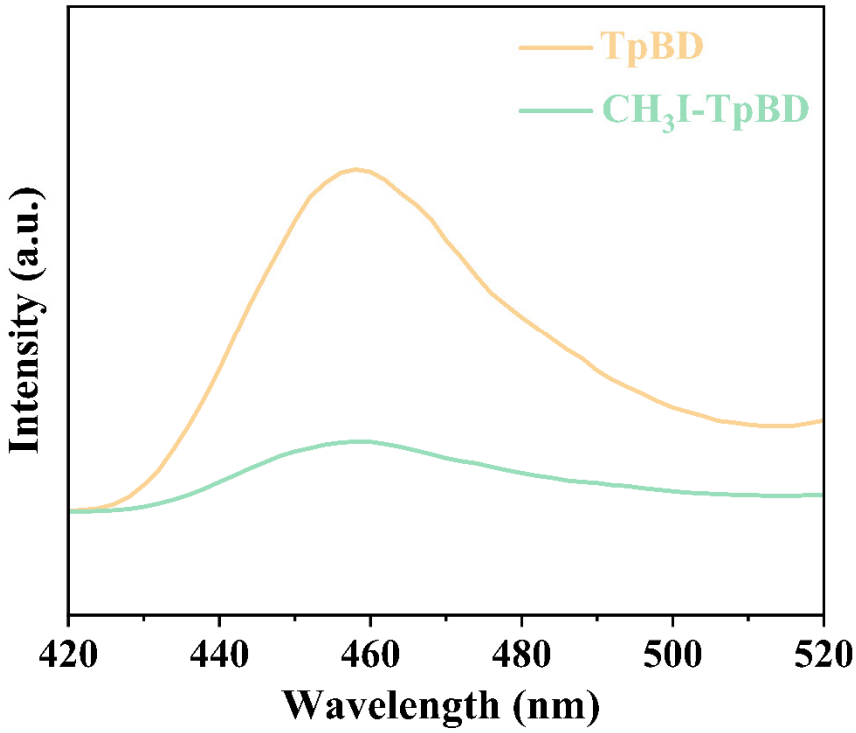


**Fig. S44:** PL spectra of TpBD and $CH_3I$-TpBD.

**Note:** The fluorescence intensity of $CH_3I$-TpBD was obviously quenched, which can be ascribe to role of built-in electric field in promoting carrier separation.

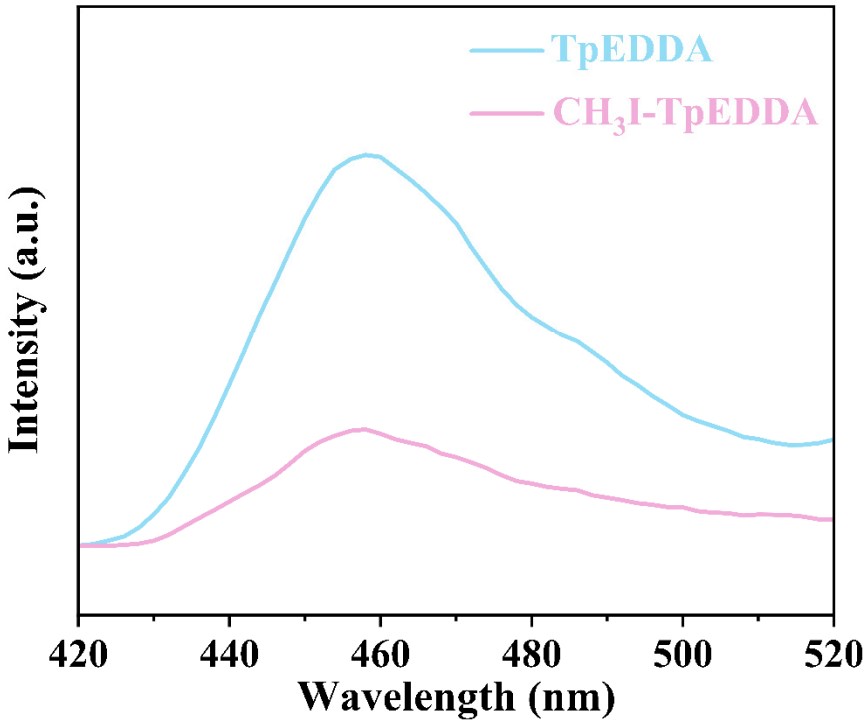


**Fig. S45:** PL spectra of TpEDDA and $CH_3I$-TpEDDA.

**Note:** The fluorescence intensity of $CH_3I$-TpEDDA was obviously quenched, which can be ascribe to role of built-in electric field in promoting carrier separation.

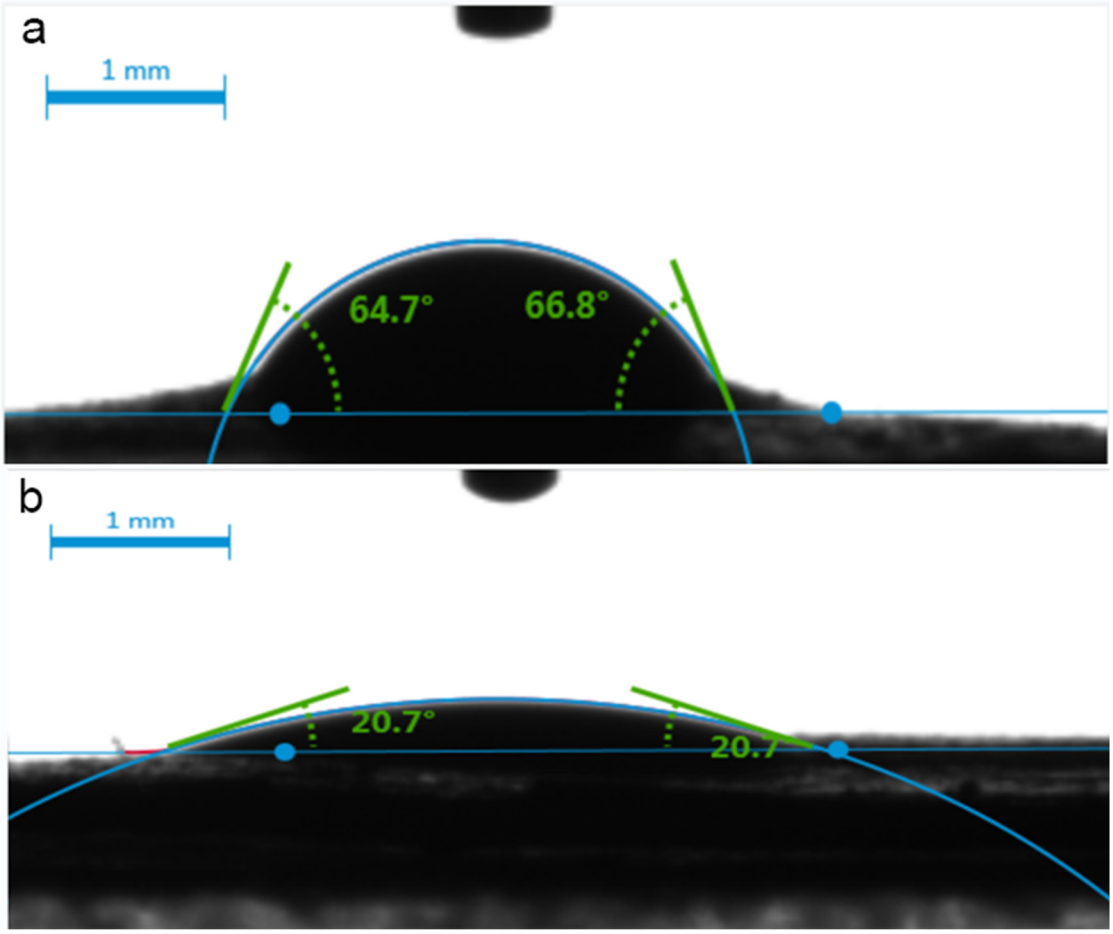


**Fig. S46:** The water contact angle of TpPa-1 and $CH_3I$-TpPa-1.

**Note:** $CH_3I$-TpPa-1 exhibited the smaller water contact angle, indicating its pronounced hydrophilicity.

**Fig. S47:** Photocatalytic Reaction Apparatus.

**Note:** The photocatalytic experiments were conducted using the Labsolar-6a, an all-glass automated online trace gas analysis system, produced by Beijing Perfectlight Technology Co., Ltd. The light source was a 300 W Xenon lamp, also manufactured by Beijing Perfectlight Technology Co., Ltd. Hydrogen detection and quantification were performed with a GC7900 gas chromatograph, manufactured by Shanghai Tianmei Scientific Instrument Co.

**Table S1** Comparison of $H_2$ evolution performance of the COFs in this work with other reported COFs materials.

| Catalysts | Cocatalyst | Illumination | Activity ($mmol \cdot g^{-1} h^{-1}$) | Ref |
|---|---|---|---|---|
| **$CH_3I$-TpPa-1** | none | λ>420nm | 9.21 | **This work** |
| **$CH_3I$-TpBD** | none | λ>420nm | 4.72 | **This work** |
| **$CH_3I$-TpEDDA** | none | λ>420nm | 2.96 | **This work** |
| N3-COF | Co-1 | AM1.5 | 0.16 | [4] |
| N2-COF | Co-1 | AM1.5 | 0.78 | [4] |
| N1-COF | Co-1 | AM1.5 | 0.1 | [4] |
| Py-CITP-BT-COF | none | λ>420nm | 2.2 | [5] |
| TpDTz-COF | none | λ>420nm | 0.94 | [6] |
| Tp-DBN | Pt | λ>420nm | 1.8 | [7] |
| Tp-PDA | Pt | λ>420nm | 0.6 | [7] |
| TFPT-COF | Pt | λ>420nm | 1.97 | [8] |
| PMDA-COF | Pt | λ>420nm | 0.44 | [9] |
| TP-BDDA | Pt | λ>395nm | 0.32 | [10] |
| PyG-COF | Pt | λ>420nm | 0.65 | [11] |
| TAB-TFP | Pt | λ>420nm | 1.14 | [12] |
| TM-DMA | Pt | λ>420nm | 4.3 | [13] |
| g-$C_{40}N_3$-COF | Pt | λ>420nm | 4.12 | [14] |
| CTF-1-100 W | Pt | λ>420nm | 5.5 | [15] |
| CTF-0-$M_2$ | Pt | λ>420nm | 4.9 | [16] |
| TpPa-COF-$(CH_3)_2$ | Pt | λ>420nm | 8.33 | [17] |
| Py-MPA | Pt | λ>420nm | 5.17 | [18] |
| PETZ-COF | Pt | λ>420nm | 7.32 | [19] |

[1] Yang, J., Jing, J., Li, W.&Zhu, Y. Electron donor–acceptor interface of TPPS/PDI boosting charge transfer for efficient photocatalytic hydrogen evolution. *Adv. Sci.* **9**, 2201134(2022).

[2] Zhang, Z., Zhu, Y., Chen, X., Zhang, H.&Wang, J. A full-spectrum metal-free porphyrin supramolecular photocatalyst for dual functions of highly efficient hydrogen and oxygen evolution. *Adv. Mater.* **31**, 1806626(2019).

[3] Pu, Z., Amiinu, I. S., Kou, Z., Li, W.&Mu, S. RuP2-based catalysts with platinum-like activity and higher durability for the hydrogen evolution reaction at all pH values. *Angew. Chem. Int. Ed.* **56**, 11559-11564(2017).

[4] Banerjee, T.et al. Single-site photocatalytic $H_2$ evolution from covalent organic frameworks with molecular cobaloxime co-catalysts. *J. Am. Chem. Soc.* **139**, 16228-16234(2017).

[5] Chen, W.et al. Modulating benzothiadiazole-based covalent organic frameworks via halogenation for enhanced photocatalytic water splitting. *Angew. Chem.* **132**, 17050-17057(2020).

[6] Biswal, B. P.et al. Sustained solar H2 evolution from a thiazolo [5, 4-d] thiazole-bridged covalent organic framework and nickel-thiolate cluster in water. *J. Am. Chem. Soc.* **141**, 11082-11092(2019).

[7] Wang, L.et al. Activation of Carbonyl Oxygen Sites in β-Ketoenamine-Linked Covalent Organic Frameworks via Cyano Conjugation for Efficient Photocatalytic Hydrogen Evolution. *Small* **17**, 2101017(2021).

[8] Stegbauer, L., Schwinghammer, K.&Lotsch, B. V. A hydrazone-based covalent organic framework for photocatalytic hydrogen production. *Chem. Sci.* **5**, 2789-2793(2014).

[9] Lu, R.et al. Effect of linkages on photocatalytic $H_2$ evolution over covalent organic frameworks. *J. Photochem. Photobiol. A: Chem.* **421**, 113546(2021).

[10] Pachfule, P.et al. Diacetylene functionalized covalent organic framework (COF) for photocatalytic hydrogen generation. , *J. Am. Chem. Soc.* **140**, 1423-1427(2018).

[11] Liu, H.et al. Post-cyclization of a bisimine-linked covalent organic framework to enhance the performance of visible-light photocatalytic hydrogen evolution. *Polym. Chem.* **14**, 1323-1329(2023).

[12] Wu, X.et al. Arylboron functional covalent organic frameworks for synergistic photocatalytic hydrogen evolution. *J. Mater. Chem. A* **10**, 17691-17698(2022).

[13] Xie, Z.et al. Vinylene-linked covalent organic frameworks with manipulated electronic structures for efficient solar-driven photocatalytic hydrogen production. *Chin. J. Catal.* **47**, 171-180(2023).

[14] Bi, S.et al. Two-dimensional semiconducting covalent organic frameworks via condensation at arylmethyl carbon atoms. *Nat. Commun.* **10**, 2467(2019).

[15] Sun, R.&Tan, B. Covalent triazine frameworks (CTFs): synthesis, crystallization, and photocatalytic water splitting. *Chem. Eur. J.* **29**, e202203077(2023).

[16] Kong, D.et al. Tunable covalent triazine-based frameworks (CTF-0) for visible-light-driven hydrogen and oxygen generation from water splitting. *ACS Catal.*

**9**, 7697-7707(2019).

[17] Sheng, J. L.et al. Effect of different functional groups on photocatalytic hydrogen evolution in covalent-organic frameworks. *ChemCatChem* **11**, 2313-2319(2019).

[18] Liu, Y.et al. One-dimensional covalent organic frameworks with atmospheric water harvesting for photocatalytic hydrogen evolution from water vapor. *Appl. Catal. B Environ.* **338**, 123074(2023).

[19] Yu, H.et al. Donor–acceptor covalent organic framework hollow submicrospheres with a hierarchical pore structure for visible-light-driven H 2 evolution. *Mater. Chem. A* **10**, 11010-11018(2022).